In vivo fluorescence resonance energy transfer imaging reveals differential activation of Rho-family GTPases in glioblastoma cell invasion

Eishu Hirata[1], Hiroko Yukinaga[2], Yuji Kamioka[1], Yoshiki Arakawa[3], Susumu Miyamoto[3], Takaharu Okada[4], Erik Sahai[5] and Michiyuki Matsuda[1,2,*]

[1]Department of Bioimaging and Cell Signaling, Graduate School of Biostudies, Kyoto University, Kyoto, 606-8501, Japan
[2]Department of Pathology and Biology of Diseases, Graduate School of Medicine, Kyoto University, Kyoto, 606-8501, Japan
[3]Department of Neurosurgery, Graduate School of Medicine, Kyoto University, Kyoto, 606-8507, Japan
[4]Research Unit for Immunodynamics, RIKEN Research Center for Allergy and Immunology, Yokohama, 230-0045, Japan
[5]Tumour Cell Biology Laboratory, Cancer Research UK London Research Institute, London, WC2A 3PX, UK
*Author for correspondence (matsudam@lif.kyoto-u.ac.jp)

Accepted 17 August 2011
Journal of Cell Science 125, 858–868

doi: 10.1242/jcs.089995

Summary

Two-photon excitation microscopy was used to visualized two different modes of invasion at perivascular and intraparenchymal regions of rat C6 glioblastoma cells that were orthotopically implanted into rat brains. Probes based on the principle of Förster resonance energy transfer (FRET) further revealed that glioblastoma cells penetrating the brain parenchyma showed higher Rac1 and Cdc42 activities and lower RhoA activity than those advancing in the perivascular regions. This spatial regulation of Rho-family GTPase activities was recapitulated in three-dimensional spheroid invasion assays with rat and human glioblastoma cells, in which multipod glioblastoma cells that invaded the gels and led the other glioblastoma cells exhibited higher Rac1 and Cdc42 activities than the trailing glioblastoma cells. We also studied the Cdc42-specific guanine nucleotide exchange factor Zizimin1 (also known as DOCK9) as a possible contributor to this spatially controlled activation of Rho-family GTPases, because it is known to play an essential role in the extension of neurites. We found that shRNA-mediated knockdown of Zizimin1 inhibited formation of pseudopodia and concomitant invasion of glioblastoma cells both under a 3D culture condition and in vivo. Our results suggest that the difference in the activity balance of Rac1 and Cdc42 versus RhoA determines the mode of glioblastoma invasion and that Zizimin1 contributes to the invasiveness of glioblastoma cells with high Rac1 and Cdc42 activities.

Key words: Glioblastoma, Invasion, Rho-family GTPase, FRET, Zizimin1 (DOCK9)

Introduction

The most common and aggressive human primary brain tumor is the glioblastoma, which invades extremely rapidly and culminates in the death of patients usually within a year after diagnosis (Louis et al., 2007). Glioblastoma was previously called glioblastoma 'multiforme', reflecting its histopathological divergence in size, shape, karyotype, etc. Glioblastomas invade either around the vascular space or along neuronal fibers into the brain parenchyma (Bellail et al., 2004; Furnari et al., 2007). Among many experimental models of human glioblastoma, the allograft model of rat C6 glioblastoma cells is used most extensively (Grobben et al., 2002). The C6 glioblastoma cells implanted into syngeneic Wistar rats share many histological hallmarks with human glioblastoma and preferentially migrate along neuronal fibers and through the perivascular region, which resembles the spread of human glioblastoma.

Various types of cancer cell exhibit diverse invasion morphologies with great plasticity not only in the tissues but also in the three-dimensional (3D) substrate (Sahai and Marshall, 2003; Friedl and Wolf, 2010). Rho-family GTPases are considered to play the central role in the regulation of invasion (Sahai et al., 2007; Croft and Olson, 2008; Sanz-Moreno et al., 2008), probably through cytoskeletal reorganization (Sahai and Marshall, 2003; Kurokawa and Matsuda, 2005; Pertz et al., 2006; Machacek et al., 2009). It has also been documented that coordinated activation and/or antagonistic action of Rho-family GTPases determine the invasion modes of various cancer cell types in the 3D environment (Sahai et al., 2007; Croft and Olson, 2008; Sanz-Moreno et al., 2008). However, the activity of Rho-family GTPases in vivo or in 3D substrate has never been successfully shown in mammals. Consequently, the spatial regulation of Rho-family GTPase in cancer tissues is unknown.

We and others have been developing biosensors based on the principle of Förster resonance energy transfer (FRET) for Ras-superfamily GTPases (Aoki and Matsuda, 2009). These biosensors, which are collectively called Ras and interacting protein chimeric unit (Raichu), have been successfully used to visualize the spatiotemporal regulation of Rho-family GTPases within MDCK cells (Kurokawa and Matsuda, 2005), zebrafish (Miyagi et al., 2004) and *Drosophila melanogaster* (Kamiyama and Chiba, 2009). However, there was a fatal flaw in the

Journal of Cell Science

application of the current FRET biosensors to 3D imaging: stable transfectants of FRET biosensors are not readily obtained when fluorescent proteins derived from *Aequorea victoria* are used as the FRET donor and acceptor proteins (Aoki and Matsuda, 2009). To circumvent this problem, we have developed FRET biosensors with a teal fluorescent protein (TFP) as a FRET donor and succeeded in establishing C6 glioblastoma cell lines expressing FRET biosensors. With these newly developed FRET biosensors, we demonstrate that two different invasion modes of glioblastoma cells can be achieved by the activity balance of Rac1 and Cdc42 versus RhoA. This spatially biased activity is at least partly dependent on Zizimin1 (also known as DOCK9), a Cdc42-specific guanine nucleotide exchange factor.

Results

Time-lapse two-photon microscopy revealed different invasion modes in the perivascular region and parenchymal tissue

C6 glioblastoma cells expressing GFP as a marker were grafted into rat brains and after 7 days were observed ex vivo by the brain slice culture technique. The transplanted C6 glioblastoma cells looked poorly delineated macroscopically (Fig. 1A). However, under a two-photon microscope, glioblastoma cells could be seen to have advanced preferentially along blood vessels at the invasion front (Fig. 1B,C), and had often penetrated the brain parenchyma from the perivascular region (arrowheads in Fig. 1C). Time-lapse images revealed that glioblastoma cells

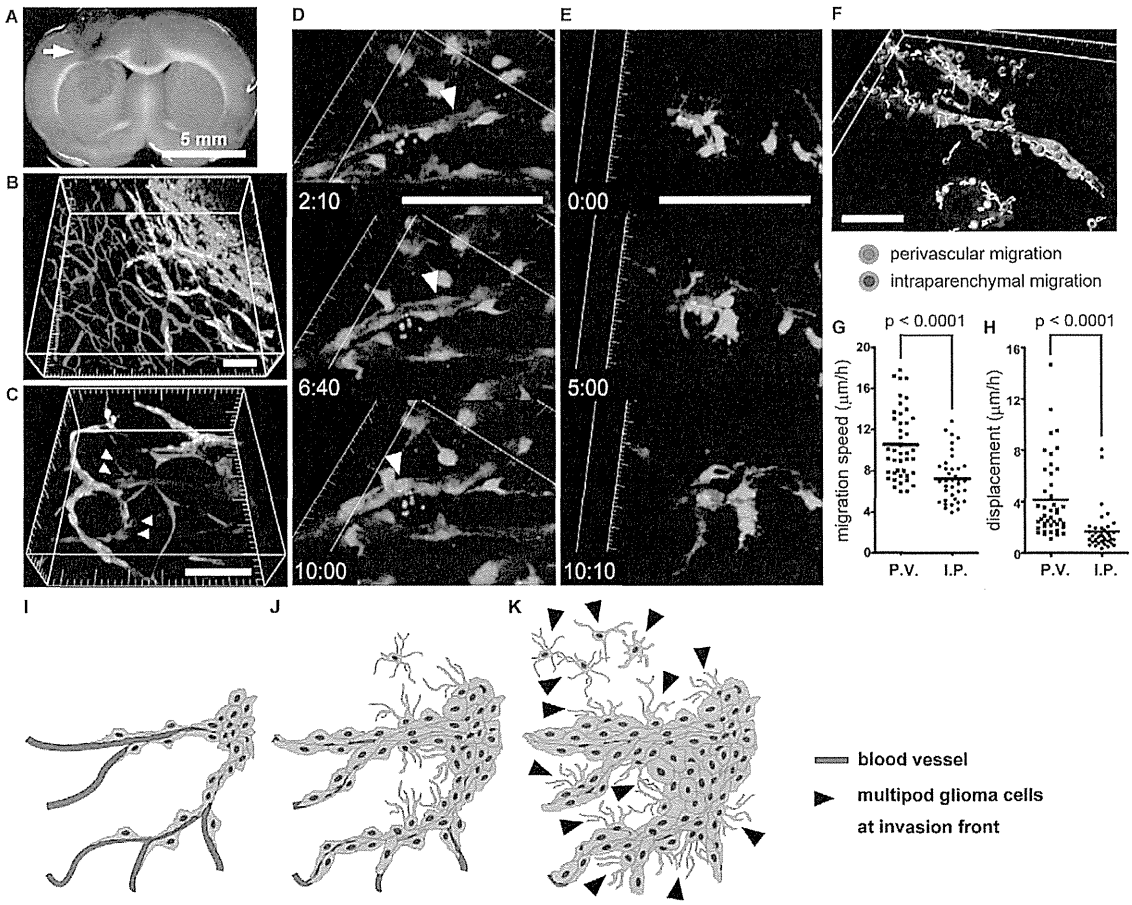

Fig. 1. Time-lapse two-photon microscopy revealed different invasion modes in the perivascular region and parenchymal tissue. (**A**) C6 glioblastoma cells stably expressing mEGFP formed an invasive tumor mass in rat brains 7 days after inoculation (arrow). (**B,C**) The invasion front of the tumor was imaged under a two-photon excitation microscope. An enlarged view is shown in C. C6 glioblastoma cells are shown in green and blood vessels, labeled with Texas-Red-conjugated dextran are red. (**D,E**) Time-lapse images revealed that the invasion morphologies of C6 glioblastoma cells in the perivascular space (D) were different from those in the parenchymal tissue (E). Blood vessels are shown in red in both figures. (**F**) Invading C6 glioblastoma cells at the periphery of the tumor mass were classified into two groups: a perivascular invasion group and intraparenchymal invasion group (colored red and blue, respectively). Time-lapse images were corrected for drift, and migration speed (μm/hour) and net displacement (μm/hour) were quantitatively analyzed, and are shown in **G** and **H**, respectively. Forty-three cells in the perivascular invasion group and 40 cells in the intraparenchymal invasion group from three independent experiments were analyzed. Bars in the scatter-plot graphs indicate the means. P.V., perivascular invasion group; I.P., intraparenchymal invasion group. (**I–K**) A hypothetical model of glioblastoma progression. Scale bars: (A) 5 mm, (B–F) 100 μm. *P*-values were calculated using unpaired *t*-tests.

migrating along blood vessels (Fig. 1D, arrowhead; supplementary material Movie 1) and those invading the brain parenchyma (Fig. 1E; supplementary material Movie 2) exhibited striking differences, not only in their morphology but also in their mode of invasion. Glioblastoma cells migrating along blood vessels were spindle shaped with a single pseudopodium extending toward the direction of movement (Fig. 1D, arrowhead; supplementary material Movie 1), but glioblastoma cells invading the brain parenchyma extended multiple pseudopodia, which continuously probed in various directions (Fig. 1E; supplementary material Movie 2). One of these protrusions then became 'favored' and determined the direction of cell invasion; however the mechanisms underlying the selection of protrusion are not known. To quantify the difference in the two invasion modes, we measured the velocity and net displacement of the glioblastoma cells in each invasion mode at the periphery of the tumor mass (Fig. 1F). Both the velocity and net displacement of glioblastoma cells migrating along the perivascular region were larger than those of glioblastoma cells invading the parenchyma (Fig. 1G,H). These observations demonstrated two modes of glioblastoma invasion: (1) glioblastoma cells advance along blood vessels straightforwardly and rapidly (Fig. 1I); (2) some glioblastoma cells penetrate the brain parenchyma, extending multiple pseudopodia (Fig. 1J) eventually filling the inter-blood vessel space (Fig. 1K).

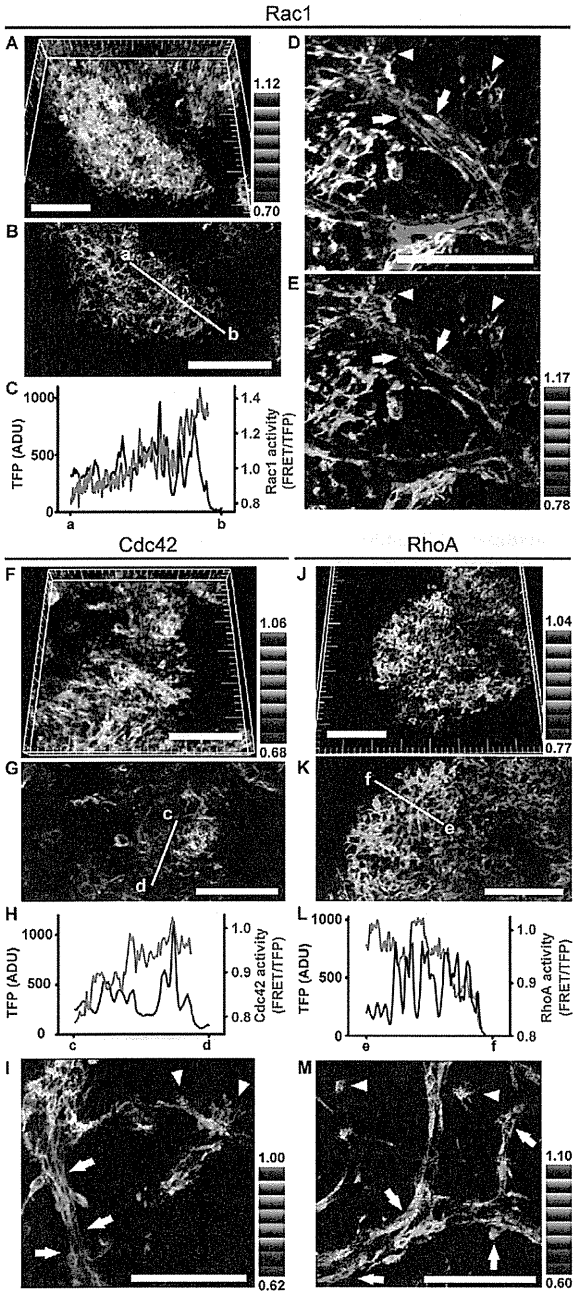

Glioblastoma cells invading the brain parenchyma showed higher Rac1 and Cdc42 activities and lower RhoA activity than those advancing in the perivascular region

To elucidate the role of Rho-family GTPases in the regulation of the two different invasion modes of glioblastoma cells, we developed new FRET biosensors that could be expressed stably in glioblastoma cells. For this purpose, we modified FRET biosensors for Rac1, Cdc42 and RhoA (Itoh et al., 2002; Yoshizaki et al., 2003) by adopting teal fluorescent protein (TFP) and a yellow fluorescent protein variant, Venus, as donor and acceptor fluorescent proteins, respectively (supplementary material Fig. S1). We found that the sensitivity and the dynamic rages of the new biosensors were almost comparable with those of the previously reported biosensors. Then, we established C6 glioblastoma cells stably expressing these biosensors, and grafted them into rat brains. Glioblastoma cells extending multiple pseudopodia at the periphery of the tumor mass grossly exhibited higher Rac1 activity than those inside the tumor mass (Fig. 2A–C), and this activity gradient was independent of the expression level of the biosensors (Fig. 2C). When viewed at higher magnification the glioblastoma cells invading the parenchyma with multiple pseudopodia (arrowheads in Fig. 2D,E) exhibited higher Rac1 activity than those

Fig. 2. Glioblastoma cells invading the brain parenchyma showed high Rac1 and Cdc42 activities. (**A–C**) C6 glioblastoma cells stably expressing the Raichu–Rac1 FRET biosensor were inoculated into rat brains, and the periphery of the tumor mass was imaged under a confocal laser scanning microscope, 7 days after inoculation. The three-dimensional reconstructed image (A) and representative section view (B) are shown in intensity-modulated display (IMD) mode with 32-intensity in 8-ratio. The gradient of the color bar shows the activity of Rac1 GTPase, with higher activity shown in red and lower activity in blue. The TFP intensity and Rac1 activity (FRET/TFP) on the section view in B was quantitatively analyzed by the line-scan method (a–b) and is shown in C. (**D,E**) An enlarged view around blood vessels from a similar experiment. The same section of glioblastoma cells is show in the mTFP channel with blood vessels in red (D) and Rac1 activity in the IMD mode (E). Images were constructed from the sum of three sequential images at 4 μm intervals. (**F–M**) C6 glioblastoma cells stably expressing Raichu–Cdc42 (F–I) or Raichu–RhoA (J–M) were analyzed using the same method. Scale bars: 100 μm.

advancing along blood vessels (arrows in Fig. 2D,E). A similar observation was obtained for Cdc42 (Fig. 2F–I). In clear contrast, RhoA activity was lower in the glioblastoma cells invading the parenchyma with multiple pseudopodia than in those advancing along blood vessels (Fig. 2J–M). To visualize the difference in the activities of Rho GTPases more clearly, we extracted Rac1-high (red) and Rac1-low (blue) signals from the IMD image (supplementary material Fig. S2B,F,J). We further quantified the FRET ratio by two methods. First, cells at the perivascular region and intraparenchymal region were marked manually and the FRET ratio (FRET/TFP) was calculated and compared (supplementary material Fig. S2C,D,G,H,K,L). Second, regions were automatically set depending on the distance from the blood vessels. The FRET ratio in each region was calculated and quantified (supplementary material Fig. S3). Both methods confirmed our observation that Rac1 and Cdc42 activities were lower and RhoA activity was higher at the perivascular region than at the intraparenchymal region, and vice versa. Although various artifacts should be taken into consideration in the intravital FRET imaging, this inverse correlation between the activities of Rac1 and Cdc42 and those of RhoA, partially ignores the possible artifacts caused by the difference in cell density, depth of tissue, etc. In short, these observations suggest two interesting possibilities. First, glioblastoma cells penetrating the parenchyma might be subjected to stimulants that activate Rac1 and Cdc42 but suppress RhoA. Second, each cell might stochastically exhibit a different level of Rho-family GTPase activities. In this scenario, cells with high Rac1 and Cdc42 but low RhoA activities penetrate the brain parenchyma, whereas cells with low Rac1 and Cdc42 but high RhoA activities persist to advance along the blood vessels.

Glioblastoma cells with higher Rac1 and Cdc42 activities guided the other glioblastoma cells with lower Rac1 and Cdc42 activities in a spheroid invasion assay

To test these two possibilities, we performed a 3D spheroid invasion assay (Gaggioli et al., 2007). C6 glioblastoma cells were cultured in suspension to form spheroids and embedded in 3D Matrigel. These C6 glioblastoma cells within the spheroid invaded into Matrigel in several directions (Fig. 3A). Interestingly, the glioblastoma cells with multiple pseudopodia led the other spindle-shaped cells during invasion (arrowheads and arrows in Fig. 3B, respectively). Magnified FRET imaging revealed that these glioblastoma cells leading the invasion had higher Rac1 activities (Fig. 3C–G; supplementary material Fig. S4 and Movie 3) and Cdc42 activities (Fig. 3H–K; supplementary material Fig. S4) than the trailing glioblastoma cells. By contrast, such intercellular divergence was not clear for RhoA activity (Fig. 3L–O; supplementary material Fig. S4). This pattern of activity gradient was similar to that found in the rat brain (Fig. 2), except that low RhoA activity in the multipod cells was not recapitulated in this spheroid invasion assay. Importantly, only a limited number of glioblastoma cells initiated the invasion of the gel, which should have been uniform in its concentration of growth factors. Therefore, these observations argue for the second hypothesis: namely, selected glioblastoma cells with higher Rac1 and Cdc42 activities invaded the gel, guiding those with lower Rac1 and Cdc42 activities. Under higher magnification, the activities of Rac1, Cdc42 and RhoA were all higher in the pseudopodia than in the cell bodies (Fig. 3P–R, respectively) as reported in conventional 2D culture dishes (Kurokawa and Matsuda, 2005). Thus, the failure to detect the intercellular divergence of RhoA activity was not due to the insensitivity of Raichu–RhoA under the 3D condition.

To verify the involvement of Rac1 and RhoA in formation of pseudopodia and invasion of gels, we performed a spheroid invasion assay in the presence of inhibitors of the Rac1 or RhoA pathway. NSC23766, which inhibits Rac1 activation, collapsed the pseudopodia and inhibited invasion of the gels (Fig. 3S, middle panel; supplementary material Movie 4). By contrast, Y27632, an inhibitor of the RhoA-dependent kinase ROCK, promoted the elongation of pseudopodia, which were thinner than those of the control cells. Notably, these pseudopodia could not accelerate the invasion (Fig. 3S, lower panel; supplementary material Movie 4). We examined the effect of NSC23766 and Y27632 on the global activities of RhoA, Rac1 and Cdc42 by pull-down analysis (supplementary material Fig. S5A). None of the Rho-family GTPases was inhibited by Y27632. NSC23766 inhibited only Rac1 activity, as expected. We also analyzed Rac1, Cdc42 and RhoA activities in the spheroid invasion assay in the presence of these inhibitors (supplementary material Fig. S5B). NSC23766 abolished glioblastoma invasion, concomitant with the global decrease in Rac1 activity. In the presence of NSC23766, the leading cells with high Cdc42 activity were lost; however, the Cdc42 activity was not altered in the central cell clusters. Y27632 did not affect the activities of RhoA, Rac1 or Cdc42. All these findings suggested that glioblastoma cells with higher Rac1 activity formed multiple pseudopodia and invaded the gel, guiding the other cells with lower Rac1 activity. The role of the RhoA–ROCK pathway was not clear in this assay.

Knockdown of Zizimin1 expression impeded formation of pseudopodia and invasion

We next looked for a guanine nucleotide exchange factor (GEF) that is responsible for the high Rac1 and Cdc42 activity in the invading glioblastoma cells with multiple pseudopodia. In preliminary shotgun transcriptome sequencing and microarray analyses, we identified GEFs for Rac1 and/or Cdc42 expressed in both C6 glioblastoma cells and human glioblastoma tissues. Among them, we focused on Zizimin1. Zizimin1 was originally identified as a Cdc42-specific GEF (Meller et al., 2002) and has been shown to regulate neurite outgrowth (Kuramoto et al., 2009). Because Cdc42 controls the formation of astrocytic processes and cell polarity in migrating astrocytes (Etienne-Manneville and Hall, 2001), and could activate Rac1 in a hierarchical manner (Nobes and Hall, 1995), Zizimin1 could cause the heterogeneity in Rac1 and/or Cdc42 activity and, thereby, the two glioblastoma invasion modes.

To investigate the possibility that Zizimin1 contributes to glioblastoma invasion, we developed C6 glioblastoma cells stably expressing three different shRNAs against rat Zizimin mRNA (Zizimin1 knockdown cells: Zizimin-KD-A, -B and -C) or control shRNA (Fig. 4A,B). A spheroid invasion assay revealed that Zizimin1 knockdown greatly inhibited the formation of pseudopodia and invasion of C6 glioblastoma cells (Fig. 4C; supplementary material Fig. S6 and Movie 5). Thus, we speculated that glioblastoma cells with high expression and/or activity of Zizimin1 exhibited high Rac1 and Cdc42 activities and guided the other glioblastoma cells. To test this possibility, C6 glioblastoma cells expressing shRNA and GFP were mixed with wild-type C6 glioblastoma cells expressing a red fluorescent protein, dKeima, to form spheroids, and embedded in

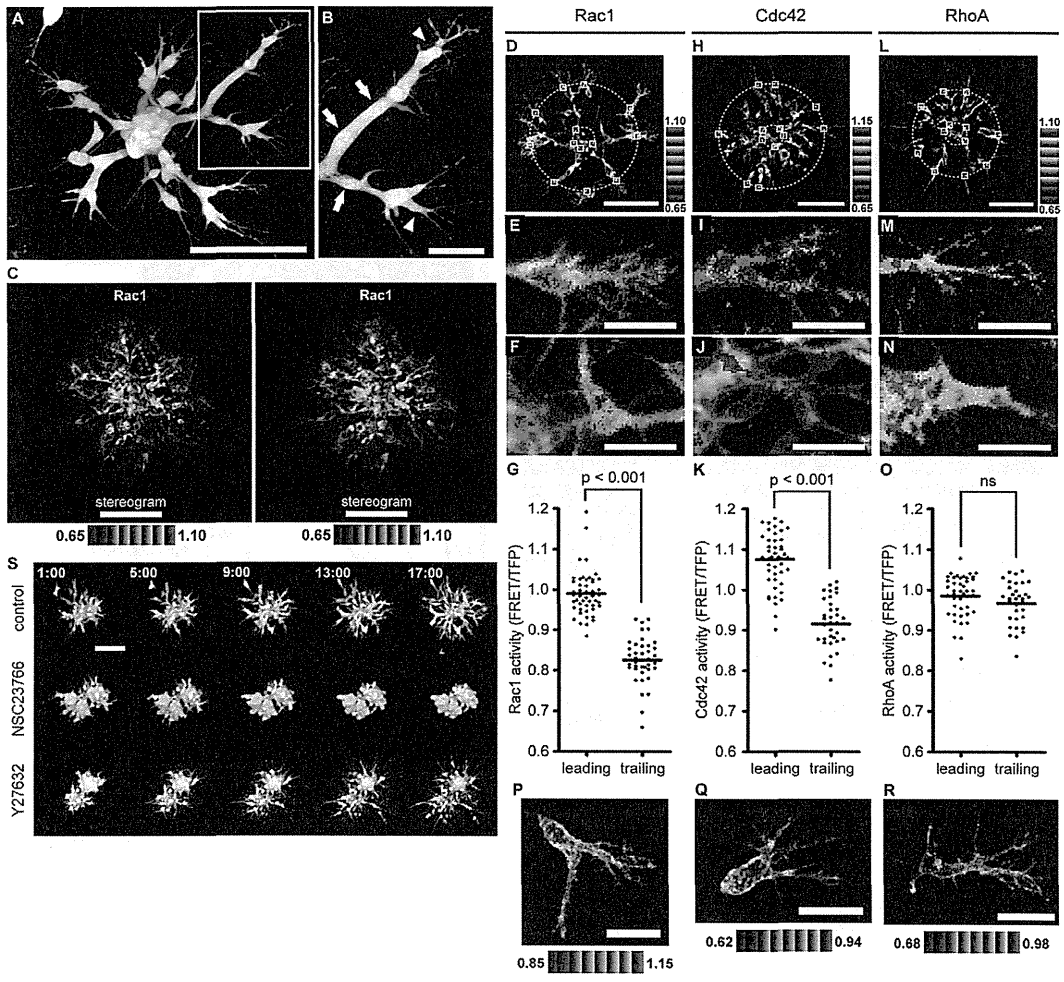

Fig. 3. High Rac1 activity was required for invasive multipod glioblastoma cells. (**A**,**B**) C6 glioblastoma cells stably expressing mEGFP were embedded in 6.0 mg/ml Matrigel and imaged under a confocal laser scanning microscope. The boxed region in A is magnified in B. (**C**) Spheroid invasion assay of C6 glioblastoma cells stably expressing the Raichu–Rac1 FRET biosensor. Cell clusters were imaged under a confocal laser scanning microscope 24 hours after being embedded in 3D Matrigel. The figures are shown in FRET IMD mode, and the two images form a stereogram for viewing by the cross-eyed method. (**D–O**) Cell clusters stably expressing Raichu–Rac1 (D), –Cdc42 (H) or –RhoA (I) were imaged and are shown in the same manner. To compare the activity (FRET/TFP ratio) of each Rho-family GTPase between cells leading invasion and cells trailing the leading cells, we set two concentric circles passing through the leading and trailing cells as shown in D,H,L. FRET images of representative cells on the outer (E,I,M) or inner circles (F,J,N) are magnified and shown. Then, square regions of interest (ROIs) of 8 by 8 pixels were set on the outer and inner circles. For each ROI, the FRET/TFP values were calculated and plotted (G,K,O). Bars in the scatter-plot graphs indicate the means. (**P–R**) FRET images focusing on the intracellular gradient of activity in Rac1 (P), Cdc42 (Q) and RhoA (R) are shown with different ratio ranges. (**S**) Spheroid invasion assay of C6 glioblastoma cells stably expressing mEGFP in the presence of the indicated reagent: NSC23766, a Rac1 inhibitor, Y27632, an inhibitor of the RhoA-dependent kinase ROCK. Image acquisition was started 1 hour after the addition of each regent. Scale bars: (A,C,D,H,L,S) 100 μm, (B,E,F,I,J,M,N,P–R) 30 μm. *P*-values were calculated using unpaired *t*-tests.

3D Matrigel. The C6 glioblastoma cells expressing the control shRNA and the wild-type C6 glioblastoma cells (green and red cells, respectively, in Fig. 4D and supplementary material Fig. S7 and Movie 6) were equally capable of forming multiple pseudopodia and invading the gel. By contrast, Zizimin1 knockdown cells (green in Fig. 4E and supplementary material Fig. S7 and Movie 6) could not invade the gels at the front, but only trailed the preceding wild-type C6 glioblastoma cells (red in the same figures and movies).

We quantified the proportion of the control and Zizimin1 knockdown cells in the leading cells in the spheroid assay (Fig. 4F). The C6 glioblastoma cells expressing the control shRNA accounted for 50% of leading cells, whereas Zizimin1 knockdown cells accounted for approximately 20%. The velocities of wild-type and Zizimin1 knockdown cells in the spheroid invasion assay were also measured for up to 16 hours (Fig. 4G,H). The wild-type C6 glioblastoma cells moved into the gels faster than the Zizimin1 knockdown cells in the first 8 hours

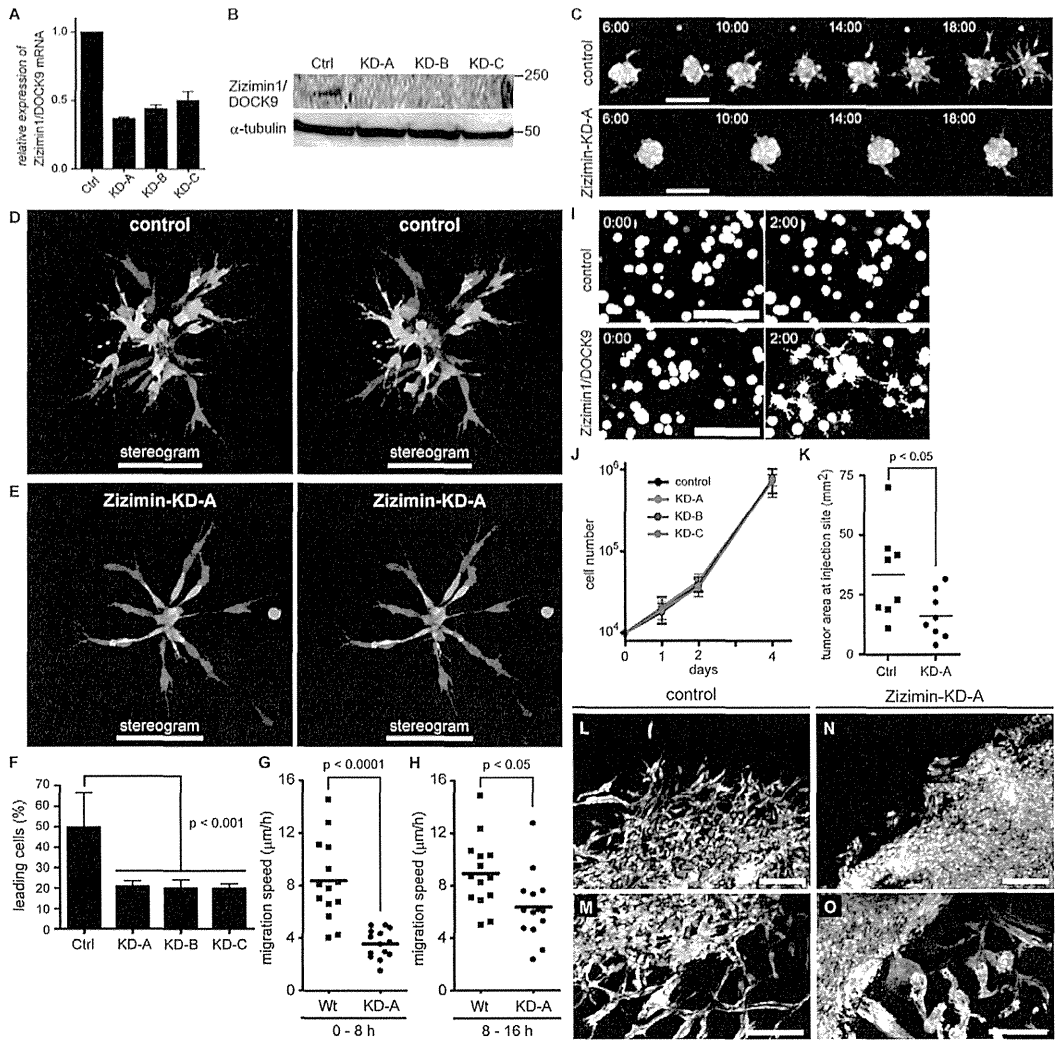

Fig. 4. Knockdown of Zizimin1 expression impeded formation of pseudopodia and invasion. (**A**,**B**) Three different shRNA-mediated RNA interference plasmids against rat Zizimin1 (Zizimin-KD-A, -B and -C) were introduced by retroviral vector into C6 glioblastoma cells stably expressing mEGFP. An shRNA targeting the firefly luciferase gene was used as a negative control. (A) The relative expression levels of Zizimin1 mRNA in the knockdown cells, as determined by quantitative RT-PCR. GAPDH was used as an internal control. Values are means ± s.d. (B) Cell lysates were subjected to SDS-PAGE and immunoblotting analysis with anti-Zizimin1 antibody and anti-α-tubulin antibody was used as a control. (**C**) Spheroid invasion assay of control (upper panel) and Zizimin1 knockdown (Zizimin-KD-A, lower panel) C6 glioblastoma cells stably expressing mEGFP in 3D Matrigel. Cell clusters were imaged under a confocal laser scanning microscope for up to 18 hours. (**D**–**H**) Control or Zizimin1 knockdown C6 glioblastoma cells stably expressing mEGFP were mixed with wild-type C6 glioblastoma cells stably expressing dKeima to form cell clusters, and embedded in 3D Matrigel. The cell clusters were imaged under a two-photon microscope 24 hours after being embedded in the gel. The two images each for D and E form a stereogram for viewing by the cross-eyed method. (F) The proportion of the control or Zizimin1 knockdown cells among the leading cells were calculated in nine independent spheroids, and are shown in a bar graph as means ± s.d. (G,H) Migration speed of wild-type C6 cells and Zizimin1 knockdown cells (Zizimin-KD-A) in the mixed spheroid invasion assay were measured in the first 8 hours (G) and in the second 8 hours (H). Each group of data consists of 14 cells from three independent experiments. Bars in the scatter-plot graphs indicate the means. (**I**) C6 glioblastoma cells stably expressing mEGFP were introduced with LDR (control; upper panels) or LDR and FKBP–Zizimin1–DHR2 (lower panels) by retroviral vector, and embedded into 3D Matrigel as single cells. The cells were treated with 50 nM rapamycin (at time 0:00) and imaged under a confocal laser scanning microscope for 2 hours. (**J**) The proliferation rates of control and Zizimin1 knockdown cells in vitro were calculated. Values are means ± s.d. (n=3). (**K**) Rat brains were inoculated with 5×10^5 control or Zizimin1 knockdown (Zizimin-KD-A) C6 glioblastoma cells, and the tumor size was analyzed 7 days after inoculation. The coronal section area at the injection site was taken as the tumor size. Bars in the scatter-plot graph indicate the means. (**L**–**O**) The peripheries of the tumor masses derived from control (H,I) or Zizimin1 knockdown (Zizimin-KD-A, J,K) C6 glioblastoma cells were imaged under a two-photon microscope. Scale bars: 100 μm. *P*-values were calculated using unpaired *t*-tests.

(Fig. 4G; supplementary material Movie 6); however, Zizimin1 knockdown cells were able to move into the gels by trailing the leading cells in the second 8 hours (Fig. 4H; supplementary material Movie 6). We examined whether the effect of shRNA could be cancelled by the expression of Zizimin1. The C6 glioblastoma cells stably expressing EGFP and shRNA against rat Zizimin1 were transfected with expression vectors of human Zizimin1 and histone-H1-conjugated mCherry, and subjected to the spheroid invasion assay (supplementary material Fig. S8). We found that 60% of the leading cells expressed the marker protein, mCherry, indicating that the effect of shRNA could be cancelled by the expression of human Zizimin1.

To further verify the role of Zizimin1 in the formation of pseudopodia in 3D gels, we developed C6 glioblastoma cells stably expressing the Lyn N-terminal sequence-tagged fragment of the mammalian target of rapamycin (LDR) and FK506 binding protein (FKBP)-fused Zizimin1 DHR2 domain (Inoue et al., 2005; Aoki et al., 2007). Rapamycin-induced membrane translocation of the DHR2 domain of Zizimin1 rapidly induced pseudopodia in C6 glioblastoma cells (Fig. 4I; supplementary material Movie 7), showing that Zizimin1 could play a pivotal role in the formation of pseudopodia through its GEF activity.

To examine whether Zizimin1 knockdown suppresses Rac1 and Cdc42 activities of C6 glioblastoma cells in the 3D spheroid invasion assay, we introduced control or Zizimin-KD-A shRNA into C6 glioblastoma cells stably expressing Raichu biosensors, and the Zizimin1 knockdown cells were marked with histone-H1-conjugated mCherry (supplementary material Fig. S9). The Zizimin1 knockdown cells were left behind and exhibited lower Rac1 and Cdc42 activities than the control cells leading the invasion. These findings suggest that Zizimin1 promotes formation of pseudopodia and concomitant invasion of C6 glioblastoma cells through Cdc42 activation in the 3D Matrigel condition.

Next, to investigate the role of Zizimin1 in glioblastoma progression in vivo, we inoculated rat brains with control or Zizimin1 knockdown glioblastoma cells. Although the Zizimin1 knockdown cells replicated as efficiently as the control cells in the culture dish (Fig. 4J), the Zizimin1 knockdown cells ostensibly grew more slowly than the control cells in brain tissues (Fig. 4K). Histologically, the control glioblastoma cells diffusely invaded the brain tissue from the perivascular region (Fig. 4L,M), whereas Zizimin1 knockdown glioblastoma cells were well demarcated from the surrounding brain tissues (Fig. 4N) and packed densely around the perivascular region (Fig. 4O). These results suggested that formation of pseudopodia by Zizimin1 was required for C6 glioblastoma cell progression in vivo, and that Zizimin1 drove glioblastoma cells around the perivascular region to invade the brain parenchyma.

Human glioblastoma cell lines also exhibited the gradient of Rac1 and Cdc42 activities and dependency on Zizimin1

To investigate whether human glioblastoma cells also exhibited a gradient of Rho-family GTPase activity during invasion of the gel, we introduced Raichu biosensors into three human glioblastoma cell lines, U251MG, LN229 and U87MG, and performed the 3D spheroid invasion assay (Fig. 5A–C). FRET microscopy revealed that cells leading the invasion exhibited higher Rac1 and Cdc42 activity than the trailing cells in all human glioblastoma cell lines. However, the intercellular gradient for RhoA activity varied depending on the cell type. The leading U251MG cells had slightly higher RhoA activity than the trailing cells (Fig. 5A); the gradient was not clear in LN229 cells (Fig. 5B); and in U87MG cells the RhoA activity of the leading cells was lower than that of the trailing cells (Fig. 5C). These findings suggest that the human glioblastoma cells with higher Rac1 and Cdc42 activity guide the other human glioblastoma cells with lower Rac1 and Cdc42 activity, as in rat C6 glioblastoma cells, and that RhoA activity might play different roles depending on the glioblastoma cells.

Next, to investigate whether Zizimin1 played an important role in human glioblastoma cell invasion as in rat C6 glioblastoma cells, we established human glioblastoma cells stably-expressing shRNA against human Zizimin1 mRNA (Fig. 5D,E). Knockdown of Zizimin1 in U251MG cells did not have any effect in the 3D spheroid invasion assay (Fig. 5F, upper panels). However, knockdown of Zizimin1 in LN229 and U87MG cells impeded formation of pseudopodia and invasion of the gel (Fig. 5G,H, respectively, upper panels). To reconstitute in vivo human glioblastoma tissue consisting of cells with various expression and/or activity levels of Zizimin1, glioblastoma cells with or without Zizimin1 shRNA were mixed to form spheroids, and a 3D invasion assay was performed. We found that Zizimin1 knockdown LN229 or U87MG cells could only follow the wild-type glioblastoma cells into the gels (Fig. 5G,H, respectively, lower panels). Again, we could not find any effect of Zizimin1 shRNA in U251MG cells (Fig. 5F, lower panels). These findings indicate that Zizimin1 also plays a pivotal role in formation of pseudopodia and invasion in some human glioblastoma cells, as in rat C6 glioblastoma cells.

Discussion

Previous histological studies have shown that C6 glioblastoma cells invade through the perivascular space and along neuronal fibers of the brain parenchyma, as do the genuine human glioblastoma cells (Grobben et al., 2002). Ex vivo time-lapse images taken with conventional fluorescence microscopy have further highlighted the importance of the perivascular growth of C6 glioblastoma cells (Farin et al., 2006). Recently, Winkler et al. used a two-photon microscope to observe the invasion of mouse glioblastoma cells and reported that the perivascular glioblastoma cells moved faster than did the glioblastoma cells in the parenchyma (Winkler et al., 2009). We also confirmed these findings for C6 glioblastoma cells by using a two-photon microscope, and further demonstrated that glioblastoma cells exhibited two distinct modes of invasion depending on whether they were located in the perivascular region or parenchyma (Fig. 1). Glioblastoma cells migrating in the perivascular region had an elongated spindle shape that is consistent with mesenchymal migration (Friedl and Wolf, 2010). By contrast, most of the glioblastoma cells in the brain parenchyma resembled normal astrocytes. Interestingly, time-lapse microscopy revealed that some glioblastoma cells dynamically changed their invasion paths from the perivascular region to the intraparenchymal region, and vice versa. These findings motivated us to examine the mechanistic aspect of the switch between the two invasive modes of glioblastoma, because flexible alteration of the two invasion modes in individual glioblastoma cells could lead to effective progression of glioblastomas.

FRET imaging demonstrated that glioblastoma cells extending multiple pseudopodia at the invasion front exhibited higher Rac1 and Cdc42 activities and lower RhoA activity compared with

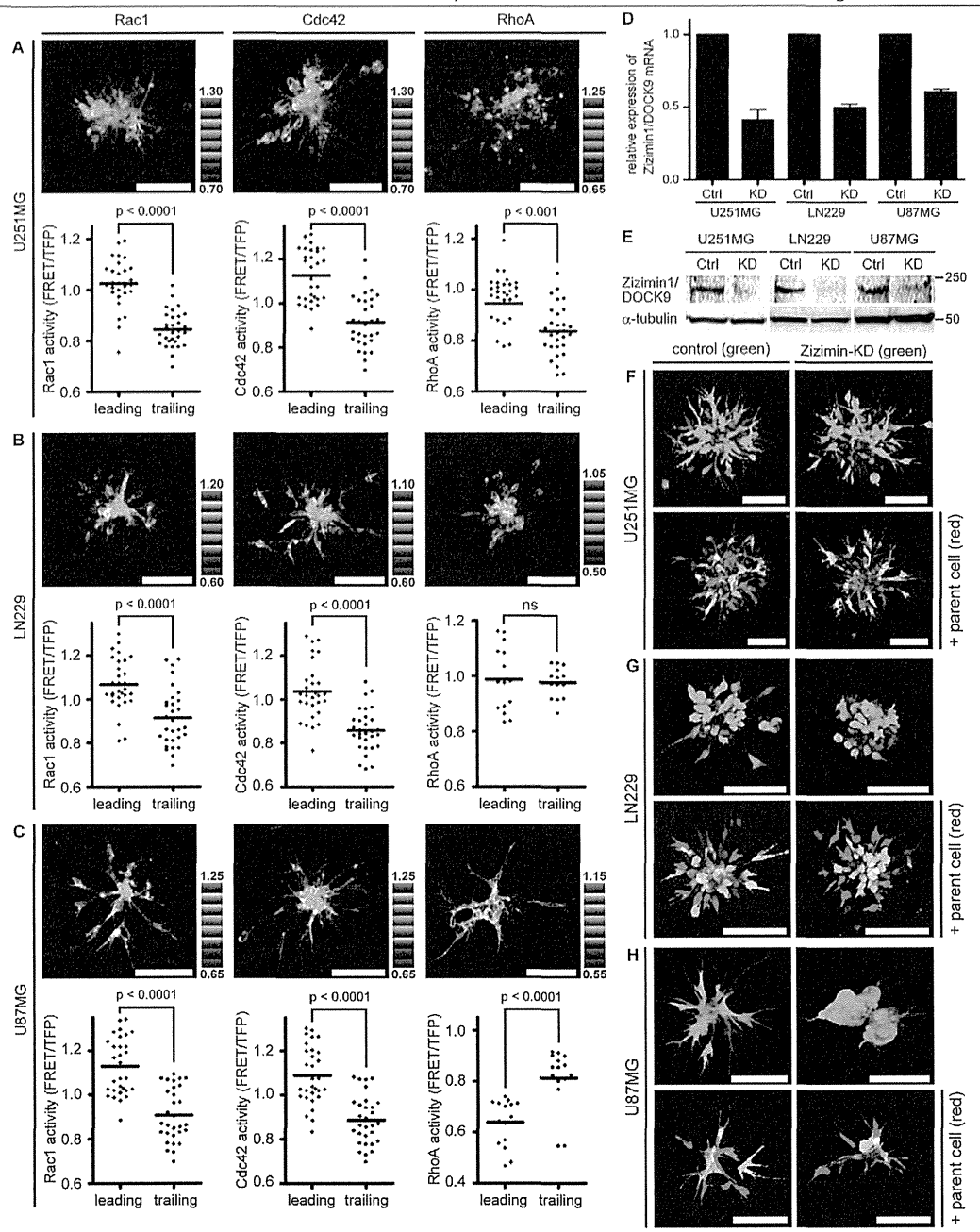

Fig. 5. Rac1 and Cdc42 activity and Zizimin1 expression in human glioblastoma correlated with their invasiveness in 3D culture. (**A–C**) Three human glioblastoma cells lines, U251MG, LN229 and U87MG, stably expressing the Raichu–Rac1, –Cdc42 and –RhoA were established and subjected to the spheroid invasion assay. Cell clusters were imaged under a confocal laser scanning microscope 36 hours (U251MG and LN229MG) or 18 hours (U87MG) after being embedded in 3D Matrigel. The activities of each GTPase are depicted in FRET IMD mode and were analyzed quantitatively as in Fig. 3. Bars in the scatter plots indicate the means. (**D**,**E**) An shRNA-mediated RNA interference plasmid against human Zizimin1 was introduced by a retroviral vector into three human glioblastoma cell lines stably expressing mEGFP. An shRNA targeting firefly luciferase transcription was used as a negative control. (D) The relative expression levels of Zizimin1 mRNA in knockdown cells as determined by quantitative RT-PCR. GAPDH was used as an internal control. Values are means ± s.d. (E) The protein expression level was examined by western blotting as in Fig. 3B. (**F–H**) Spheroid invasion assay of control and Zizimin1 knockdown cells (upper panels). Cell clusters were imaged under a confocal laser scanning microscope 36 hours (U251MG and LN229MG) or 18 hours (U87MG) after being embedded in 3D Matrigel. In other experiments (lower panels), shRNA-carrying cells labeled with GFP were mixed with the parent cells labeled with dKeima to form cell clusters, and embedded in 3D Matrigel. The cell clusters were imaged under a two-photon microscope 36 hours (U251MG and LN229MG) or 18 hours (U87MG) after being embedded in the gel. Scale bars: 100 μm. *P*-values were calculated using unpaired *t*-tests.

glioblastoma cells at the perivascular region (Fig. 2). To the best of our knowledge, this is the first report to show the intercellular activity gradient of small GTPases in living cancer tissues, although previous studies using inhibitors and mutants have suggested that the differential use of Rho-family GTPases determines the mode of cancer cell invasion (Sahai and Marshall, 2003; Sanz-Moreno et al., 2008; Yamazaki et al., 2009; Friedl and Wolf, 2010). The gradient of Rho-family GTPase activity within the glioblastoma tissue strongly supports the idea that the two glioblastoma invasion modes are correlated with the activities of Rho-family GTPases. Interestingly, recent studies by Panopoulos et al. showed that mesenchymal migration of glioblastoma cells does not require Rac1 activity on 2D substrates (Panopoulos et al., 2011). This observation suggests that glioblastoma cells do not require Rac1 activity to move without marked resistance on dishes or around blood vessels. At the same time, our observations suggested two scenarios for the increased Rac1 and Cdc42 activities: high activities of Rac1 and Cdc42 might be induced within cells invading the brain parenchyma, or cells with high Rac1 and Cdc42 activities might be driven from the perivascular space into the parenchyma.

Three lines of evidence from the 3D invasion assay support the second scenario, i.e. C6 glioblastoma cells with high Rac1 and Cdc42 activities preferentially invade the parenchyma. First, we found that C6 glioblastoma cells with high Rac1 and Cdc42 activities guided the other cells to invade the gel (Fig. 3; supplementary material Fig. S4). Second, inhibition of Rac1 activity by NSC23766 reduced the size and number of pseudopodia and suppressed the invasion (Fig. 3S; supplementary material Movie 4). We confirmed this observation with C6 glioblastoma cells expressing a dominant-negative mutant of Rac1 (data not shown). Third, Zizimin1 knockdown decreased the Rac1 and Cdc42 activities, reduced the number of cellular protrusions in C6 glioblastoma cells and suppressed the invasion in 3D Matrigel cultures (Fig. 4; supplementary material Figs S7 and S9). Intriguingly, cells with reduced Zizimin1 expression could follow the wild-type C6 glioblastoma cells in 3D culture, indicating that high Cdc42 activity is required for the invasion of the gel but not for the migration itself (Fig. 4G,H; supplementary material Movie 6).

We previously reported that Rac1 and Cdc42 activities are high in lamellipodia (Itoh et al., 2002). Thus, cells with multiple pseudopodia could contribute to high Rac1 and Cdc42 activities in cells at the invasion front. However, as shown in the magnified FRET images (Fig. 3), the leading cells exhibited high Rac1 and Cdc42 activities not only in the pseudopodia but also in the cell bodies, in comparison with the trailing cells. Thus, we concluded that the high Rac1 and Cdc42 activities in the leading cells were not caused by the presence of multiple pseudopodia.

The relevance of our finding to the development of human glioblastoma is partially validated by the use of human glioblastoma cell lines. We found that invasion-leading cells exhibited higher Rac1 and Cdc42 activity than the trailing cells in human glioblastoma cells (Fig. 5A–C), as in rat C6 glioblastoma cells, and that knockdown of Zizimin1 in LN229 and U87MG cells impeded cell invasion of the gel (Fig. 5G,H). Because knockdown of Zizimin1 in U251MG cells did not alter the invasive phenotype, we consider that the contribution of Zizimin1 to glioblastoma cell invasion might be cell-type dependent. In fact, C6, LN229 and U87MG cells expressing shRNA against Zizimin1 were found to still be capable of invading the gel when examined for longer times (data not shown), suggesting that there are other molecules cooperating with or substituting for Zizimin1. Notably, using fluorescence-based cell sorting analysis and a pull-down assay (data not shown), knockdown of Zizimin1 was not found to affect the activities of Rac1 and Cdc42 in the C6 glioblastoma cells grown on culture dishes. This observation strongly suggests that the role played by Zizimin1 is specific to the glioblastoma cells growing in 3D conditions. In addition, although Zizimin1 is highly expressed in brain (Meller et al., 2002), we found that it is not upregulated in human glioblastoma cells compared with normal brain tissue (data not shown). To the best of our knowledge, there is no previous report showing a positive or negative correlation between the Zizimin1 mRNA expression level and cell proliferation, cell invasion or the prognosis of glioblastoma patients (Phillips et al., 2006; Shirahata et al., 2007). Therefore, we could speculate that Zizimin1 might be regulated primarily by the protein activity rather than by the gene expression in glioblastoma cells and that a glioblastoma cell population should contain a small fraction of cells with high Zizimin1 activity that is highly invasive in brain parenchyma. Actually, in our observations of rat brain, only a small number of glioblastoma cells produced multiple pseudopodia and penetrated brain parenchyma (Fig. 1), as was reported in a previous study in which only a small fraction (~5%) of cancer cells showed high invasiveness in vivo (Giampieri et al., 2009).

In summary, we demonstrated that invasion modes of glioblastoma cells can be controlled by the balance of the activity of Rho-family GTPases and a Cdc42-specific GEF, and Zizimin1 appears to play an important role in the formation of multiple pseudopodia and in invasion of the brain parenchyma. Our results provide further information about the nature of heterogeneity in cancer cell populations that are composed of various cells with different fingerprints of invasiveness.

Materials and Methods

Probes and cell lines

C6 rat glioblastoma cells, U251MG, LN229 and U87MG human glioblastoma cells, and Cos7 African green monkey SV40-transformed kidney fibroblast cells were obtained from the American Type Culture Collection and cultured in DMEM containing 10% FBS. The prototype FRET biosensors for Rac1, RhoA and Cdc42 were described previously (Itoh et al., 2002; Yoshizaki et al., 2003). In the Raichu–Rac1 biosensor (2227x), Raichu–Cdc42 biosensor (2219x) and Raichu–RhoA biosensor (1523x) used in this study, CFP was replaced with the teal fluorescent protein as described previously (Yoshiki et al., 2010). A pCX4 retroviral vector was used to express the FRET biosensors and fluorescent proteins in each glioblastoma cell line as described previously (Takaya et al., 2007). The infected cells were single-cell cloned before further experiments unless described otherwise.

Intracranial transplantation of glioblastoma cells and brain slice culture

All animal care measures and experiments complied with Japanese community standards on the care and use of laboratory animals, which were approved by Kyoto University. C6 glioblastoma cells (5×10^5 cells/5 μl PBS) were stereotactically transplanted into the right subcortex of 3-week-old male Wistar rats. After 7 days, tumor-bearing rats were killed with carbon dioxide and sodium pentobarbital, and decapitated. In preliminary experiments, Texas-Red-conjugated dextran (70 kDa; Invitrogen, Carlsbad, CA) was injected into the left ventricle before decapitation to visualize blood vessels; however, we omitted this process in later experiments because we could easily distinguish blood vessels by the morphologies and distribution of cells at invasion borders. The whole brains were quickly removed, cut vertically and mounted on the stage of a Vibroslice Tissue Cutter (Campden Instruments, Loughborough, UK) filled with ice-cold artificial cerebrospinal fluid containing 135 mM *N*-methyl-D-glucamine, 1 mM KCl, 1.2 mM KH_2PO_4, 20 mM choline bicarbonate, 10 mM glucose, 1.5 mM $MgCl_2$ and 0.5 mM $CaCl_2$. Coronal brain slices (300 μm thick) were cut and transferred onto a plastic coverslip and incubated in slice culture medium at 37°C in a humidified atmosphere containing 5% CO_2 as described previously (Tanaka et al.,

2008). The slice culture medium consisted of 77% MEM, 20% HBSS, 3% HEPES, 6.5 mg/ml glucose, 6.5 mg/ml L-glutamine and N2 supplement (all from Invitrogen). For tumor size calculation, brain samples were prepared by perfusion fixation. A coronal section at the injection site was prepared for each sample and imaged under a fluorescence stereomicroscope (Carl Zeiss Meditec Inc., Dublin, CA).

Two-photon excitation microscopy and confocal laser scanning microscopy

Cultured brain slices were maintained in an incubation chamber (Tokai Hit, Shizuoka, JAPAN) and imaged using a 20× water-immersion objective (XLUMPLFL20; Olympus Optical Co., Tokyo, Japan) on a BX61WI/FV1000 upright microscope (Olympus) equipped with a 440 nm laser diode (Olympus) and a Mai-Tai Ti:sapphire laser (Spectra Physics, Mountain View, CA). The excitation wavelength for two-photon excitation was 850 nm. We used a RDM650 IR-cut filter, a DM570 dichroic mirror and two emission filters: BA510-550 for GFP and BA570-625 for Keima or Texas Red, respectively. All filters were purchased from Olympus. For FRET imaging with a confocal laser scanning unit, we used a 440 nm laser diode and the following filter sets purchased from Olympus: an excitation dichroic mirror, DM405-440/515, a second dichroic mirror, SDM510, and two emission filters, BA465-495 for TFP and BA520-550 for FRET. To obtain the intensity profile of the Raichu biosensors, we used the FV1000 lambda-scan program with a 440 nm laser diode and a beam splitter BS/20/80 (Olympus), and an SPD (Olympus) emission detecting system. Fluorescence intensities at every 5 nm wavelength with 10 nm bandwidth were obtained from 470 nm to 550 nm.

Image processing

Acquired images were analyzed with MetaMorph software (Universal Imaging, West Chester, PA). For 3D reconstruction of the images and calculation of the cell migration speed in a 3D environment, the original confocal images were analyzed with Imaris Software (Bitplane AG, Zürich, Switzerland). The tumor area was calculated according to the fluorescence signal with MetaMorph software.

Invasion assays

The organotypic culture system was set up as previously described (Gaggioli et al., 2007). Briefly, cells were embedded in Matrigel (BD Biosciences, Bedford, MA) at a concentration of approximately 6 mg/ml. For spheroid invasion assays, 1×10^6 cells in 1 ml serum-free CO_2-independent medium (Invitrogen) were agitated overnight in a 12-well plate coated with poly(2-hydroxyethyl methacrylate) (Sigma, St. Louis, MO) to form small aggregates. The aggregates were embedded in Matrigel, maintained in complete medium and observed under a two-photon or a confocal microscope for up to 18 hours in an incubation chamber. Y27632 and NSC23766 were obtained from Calbiochem (La Jolla, CA) and used at final concentrations of 20 μM and 100 μM, respectively.

shRNA-mediated knockdown of Zizimin1 and quantitative RT-PCR

pSuper.retro.puro vector (OligoEngine, Seattle, WA) was used for the expression of short hairpin RNA (shRNA). shRNAs for rat Zizimin1 were kind gifts from Hironori Katoh, Graduate School of Biostudies, Kyoto University (Kuramoto et al., 2009). An shRNA for human Zizimin1 (5′-TGGTTCCGGTTTAGATAGCTA-3′) was obtained from the Genome Network Project at the University of Tokyo (http://gnp.rnai.jp/). shRNA targeting firefly luciferase transcription (5′-GATTATGTCCGGTTATGTA-3′) was used as a negative control. The efficiency of knockdown was determined by quantitative RT-PCR. Second-derivative maximum method was applied for crossing-point determination using LightCycler version 3.3 software (Roche, Basel, Switzerland) (Hirata et al., 2009). GAPDH was used as an internal control. The following primer sets were used: for rat Zizimin1, forward 5′-CATGCAGGATGTCCATTTCA-3′, and reverse 5′-CGTGTCATACAGGTGGGCTA-3′; for rat *GAPDH*, forward 5′-GAGTC-TACTGGCGTCTTCAC-3′, and reverse 5′-GTTCACACCCATCACAAACA-3′; for human Zizimin1, forward 5′-TCCGTGTAGTGTGCAACCAT-3′, and reverse 5′-CAGTCCCACCAAGAAGTGGT-3′; for human *GAPDH*, forward 5′-GAGTCCACTGGCGTCTTCAC-3′, and reverse 5′-GTTCACACCCATGACG-AACA-3′. The conditions for PCR were 45 cycles of 95℃ for 10 seconds for denaturation, 56℃ for 10 seconds for annealing and 72℃ for 10 seconds for extension.

Pull-down assay and immunoblotting

The activities of Rac1, Cdc42 and RhoA in C6 glioblastoma cells were measured by the Bos' pull-down method (Aoki et al., 2005). Briefly, cells were harvested in ice-cold lysis buffer (50 mM Tris, pH 7.5, 100 mM NaCl, 2 mM $MgCl_2$, 1% Nonidet P-40, 10% glycerol, 1 mM dithiothreitol) containing GST–PAK–CRIB for Rac1 and Cdc42 or Rhotekin–RBD for RhoA. The cleared lysates were incubated with glutathione–Sepharose beads for 30 minutes at 4℃. The washed beads were boiled in sample buffer, and both the bound proteins and total cell lysates were analyzed by SDS-PAGE followed by immunoblotting. Precast SDS–polyacrylamide gels were purchased from Wako Pure Chemical Industries (Tokyo, Japan). Bound antibodies were detected with secondary antibodies conjugated with IRDye680 or IRDye800 and analyzed with an Odyssey Imager system (LICOR, Lincoln, NE). Anti-Rac1 and anti-Cdc42 mouse monoclonal antibodies were purchased from BD Transduction Laboratory (San Diego, CA). Anti-RhoA mouse monoclonal antibody was purchased from Santa Cruz Biotechnology (Santa Cruz, CA). Anti-human DOCK9 mouse monoclonal antibody was a kind gift from Martin A. Schwartz (Yale University) and anti α-tubulin mouse monoclonal antibody was purchased from Calbiochem.

Statistical analysis

When two groups were compared, a two-tailed unpaired Student's *t*-test was applied.

Acknowledgements

We thank H. Katoh, A. Miyawaki, T. Akagi, J. Miyazaki and M. A. Schwartz for the plasmids and antibodies. Y. Inaoka, K. Hirano, R. Sakai and N. Nonaka are also to be thanked for their technical assistance. We are grateful to the members of the Matsuda Laboratory for their helpful discussions.

Funding

This work was supported by a Sagawa Cancer Research Grant [awarded in 2008 to M.M.]; the Research Program of Innovative Cell Biology by Innovative Technology (Cell Innovation) from the Ministry of Education, Culture, Sports and Science (MEXT), Japan to M.M.; and the Global Center of Excellence Program "Center for Frontier Medicine" initiated by Ministry of Education, Culture, Sports and Science, Japan.

Supplementary material available online at
http://jcs.biologists.org/lookup/suppl/doi:10.1242/jcs.089995/-/DC1

References

Aoki, K. and Matsuda, M. (2009). Visualization of small GTPase activity with fluorescence resonance energy transfer-based biosensors. *Nat. Protoc.* **4**, 1623-1631.

Aoki, K., Nakamura, T., Fujikawa, K. and Matsuda, M. (2005). Local phosphatidylinositol 3,4,5-trisphosphate accumulation recruits Vav2 and Vav3 to activate Rac1/Cdc42 and initiate neurite outgrowth in nerve growth factor-stimulated PC12 cells. *Mol. Biol. Cell* **16**, 2207-2217.

Aoki, K., Nakamura, T., Inoue, T., Meyer, T. and Matsuda, M. (2007). An essential role for the SHIP2-dependent negative feedback loop in neuritogenesis of nerve growth factor-stimulated PC12 cells. *J. Cell Biol.* **177**, 817-827.

Bellail, A. C., Hunter, S. B., Brat, D. J., Tan, C. and Van Meir, E. G. (2004). Microregional extracellular matrix heterogeneity in brain modulates glioma cell invasion. *Int. J. Biochem. Cell Biol.* **36**, 1046-1069.

Croft, D. R. and Olson, M. F. (2008). Regulating the conversion between rounded and elongated modes of cancer cell movement. *Cancer Cell* **14**, 349-351.

Etienne-Manneville, S. and Hall, A. (2001). Integrin-mediated activation of Cdc42 controls cell polarity in migrating astrocytes through PKCzeta. *Cell* **106**, 489-498.

Farin, A., Suzuki, S. O., Weiker, M., Goldman, J. E., Bruce, J. N. and Canoll, P. (2006). Transplanted glioma cells migrate and proliferate on host brain vasculature: a dynamic analysis. *Glia* **53**, 799-808.

Friedl, P. and Wolf, K. (2010). Plasticity of cell migration: a multiscale tuning model. *J. Cell Biol.* **188**, 11-19.

Furnari, F. B., Fenton, T., Bachoo, R. M., Mukasa, A., Stommel, J. M., Stegh, A., Hahn, W. C., Ligon, K. L., Louis, D. N., Brennan, C. et al. (2007). Malignant astrocytic glioma: genetics, biology, and paths to treatment. *Genes Dev.* **21**, 2683-2710.

Gaggioli, C., Hooper, S., Hidalgo-Carcedo, C., Grosse, R., Marshall, J. F., Harrington, K. and Sahai, E. (2007). Fibroblast-led collective invasion of carcinoma cells with differing roles for RhoGTPases in leading and following cells. *Nat. Cell Biol.* **9**, 1392-1400.

Giampieri, S., Manning, C., Hooper, S., Jones, L., Hill, C. S. and Sahai, E. (2009). Localized and reversible TGFbeta signalling switches breast cancer cells from cohesive to single cell motility. *Nat. Cell Biol.* **11**, 1287-1296.

Grobben, B., De Deyn, P. P. and Slegers, H. (2002). Rat C6 glioma as experimental model system for the study of glioblastoma growth and invasion. *Cell Tissue Res.* **310**, 257-270.

Hirata, E., Arakawa, Y., Shirahata, M., Yamaguchi, M., Kishi, Y., Okada, T., Takahashi, J. A., Matsuda, M. and Hashimoto, N. (2009). Endogenous tenascin-C enhances glioblastoma invasion with reactive change of surrounding brain tissue. *Cancer Sci.* **100**, 1451-1459.

Inoue, T., Heo, W. D., Grimley, J. S., Wandless, T. J. and Meyer, T. (2005). An inducible translocation strategy to rapidly activate and inhibit small GTPase signaling pathways. *Nat. Methods* **2**, 415-418.

Itoh, R. E., Kurokawa, K., Ohba, Y., Yoshizaki, H., Mochizuki, N. and Matsuda, M. (2002). Activation of rac and cdc42 video imaged by fluorescent resonance energy

transfer-based single-molecule probes in the membrane of living cells. *Mol. Cell. Biol.* **22**, 6582-6591.

Kamiyama, D. and Chiba, A. (2009). Endogenous activation patterns of Cdc42 GTPase within Drosophila embryos. *Science* **324**, 1338-1340.

Kuramoto, K., Negishi, M. and Katoh, H. (2009). Regulation of dendrite growth by the Cdc42 activator Zizimin1/Dock9 in hippocampal neurons. *J. Neurosci. Res.* **87**, 1794-1805.

Kurokawa, K. and Matsuda, M. (2005). Localized RhoA activation as a requirement for the induction of membrane ruffling. *Mol. Biol. Cell* **16**, 4294-4303.

Louis, D. N., Ohgaki, H., Weistler, O. D. and Cavenee, W. K. (2007). *WHO Classification of Tumours of the Central Nervous System*. Switzlerland: World Health Organization Press.

Machacek, M., Hodgson, L., Welch, C., Elliott, H., Pertz, O., Nalbant, P., Abell, A., Johnson, G. L., Hahn, K. M. and Danuser, G. (2009). Coordination of Rho GTPase activities during cell protrusion. *Nature* **461**, 99-103.

Meller, N., Irani-Tehrani, M., Kiosses, W. B., Del Pozo, M. A. and Schwartz, M. A. (2002). Zizimin1, a novel Cdc42 activator, reveals a new GEF domain for Rho proteins. *Nat. Cell Biol.* **4**, 639-647.

Miyagi, C., Yamashita, S., Ohba, Y., Yoshizaki, H., Matsuda, M. and Hirano, T. (2004). STAT3 noncell-autonomously controls planar cell polarity during zebrafish convergence and extension. *J. Cell Biol.* **166**, 975-981.

Nobes, C. D. and Hall, A. (1995). Rho, rac, and cdc42 GTPases regulate the assembly of multimolecular focal complexes associated with actin stress fibers, lamellipodia, and filopodia. *Cell* **81**, 53-62.

Panopoulos, A., Howell, M., Fotedar, R. and Margolis, R. L. (2011). Glioblastoma motility occurs in the absence of actin polymer. *Mol. Biol. Cell* **22**, 2212-2220.

Pertz, O., Hodgson, L., Klemke, R. L. and Hahn, K. M. (2006). Spatiotemporal dynamics of RhoA activity in migrating cells. *Nature* **440**, 1069-1072.

Phillips, H. S., Kharbanda, S., Chen, R., Forrest, W. F., Soriano, R. H., Wu, T. D., Misra, A., Nigro, J. M., Colman, H., Soroceanu, L. et al. (2006). Molecular subclasses of high-grade glioma predict prognosis, delineate a pattern of disease progression, and resemble stages in neurogenesis. *Cancer Cell* **9**, 157-173.

Sahai, E. and Marshall, C. J. (2003). Differing modes of tumour cell invasion have distinct requirements for Rho/ROCK signalling and extracellular proteolysis. *Nat. Cell Biol.* **5**, 711-719.

Sahai, E., Garcia-Medina, R., Pouyssegur, J. and Vial, E. (2007). Smurf1 regulates tumor cell plasticity and motility through degradation of RhoA leading to localized inhibition of contractility. *J. Cell Biol.* **176**, 35-42.

Sanz-Moreno, V., Gadea, G., Ahn, J., Paterson, H., Marra, P., Pinner, S., Sahai, E. and Marshall, C. J. (2008). Rac activation and inactivation control plasticity of tumor cell movement. *Cell* **135**, 510-523.

Shirahata, M., Iwao-Koizumi, K., Saito, S., Ueno, N., Oda, M., Hashimoto, N., Takahashi, J. A. and Kato, K. (2007). Gene expression-based molecular diagnostic system for malignant gliomas is superior to histological diagnosis. *Clin. Cancer Res.* **13**, 7341-7356.

Takaya, A., Kamio, T., Masuda, M., Mochizuki, N., Sawa, H., Sato, M., Nagashima, K., Mizutani, A., Matsuno, A., Kiyokawa, E. et al. (2007). R-Ras regulates exocytosis by Rgl2/Rlf-mediated activation of RalA on endosomes. *Mol. Biol. Cell* **18**, 1850-1860.

Tanaka, Y., Tanaka, Y. Furuta, T., Yanagawa, Y. and Kaneko, T. (2008). The effects of cutting solutions on the viability of GABAergic interneurons in cerebral cortical slices of adult mice. *J. Neurosci. Methods* **171**, 118-125.

Winkler, F., Kienast, Y., Fuhrmann, M., Von Baumgarten, L., Burgold, S., Mitteregger, G., Kretzschmar, H. and Herms, J. (2009). Imaging glioma cell invasion in vivo reveals mechanisms of dissemination and peritumoral angiogenesis. *Glia* **57**, 1306-1315.

Yamazaki, D., Kurisu, S. and Takenawa, T. (2009). Involvement of Rac and Rho signaling in cancer cell motility in 3D substrates. *Oncogene* **28**, 1570-1583.

Yoshiki, S., Matsunaga-Udagawa, R., Aoki, K., Kamioka, Y., Kiyokawa, E. and Matsuda, M. (2010). Ras and calcium signaling pathways converge at Raf1 via the Shoc2 scaffold protein. *Mol. Biol. Cell* **21**, 1088-1096.

Yoshizaki, H., Ohba, Y., Kurokawa, K., Itoh, R. E., Nakamura, T., Mochizuki, N., Nagashima, K. and Matsuda, M. (2003). Activity of Rho-family GTPases during cell division as visualized with FRET-based probes. *J. Cell Biol.* **162**, 223-232.

J Neurooncol (2012) 109:425–432
DOI 10.1007/s11060-012-0912-6

CLINICAL STUDY

Outcomes of hypofractionated stereotactic radiotherapy for metastatic brain tumors with high risk factors

Kengo Ogura · Takashi Mizowaki · Masakazu Ogura · Katsuyuki Sakanaka · Yoshiki Arakawa · Susumu Miyamoto · Masahiro Hiraoka

Received: 3 December 2011 / Accepted: 4 June 2012 / Published online: 20 June 2012

Abstract The present study aimed to analyze outcomes of hypofractionated stereotactic radiotherapy (HFSRT) delivered in five fractions to metastatic brain tumors. Between June 2008 and June 2011, 39 consecutive patients with 46 brain metastases underwent HFSRT at Kyoto University Hospital. Selection criteria included high risk factors such as eloquent location, history of whole-brain radiotherapy (WBRT), or large tumor size. Given these factors, fractionated schedules were preferable in terms of radiobiology. The prescribed dose at the isocenter was basically 35 Gy in five fractions. Brainstem lesions with a history of WBRT were treated with 20–25 Gy in five fractions. Planning target volume was covered by the 80 % isodose line of the prescribed dose to the isocenter. Local-control probability and overall survival were estimated using the Kaplan–Meier method. For the analysis of local control, the response criteria were defined as follows: complete response (CR) was defined as no visible gross tumor or absence of contrast enhancement, partial response (PR) as more than a 30 % decrease in size, progressive disease as more than a 20 % increase in size, and stable disease (SD) as all other responses. Local control was defined as a status of CR, PR, or SD. Only patients with at least 3 months or longer follow-up (21 patients, 27 tumors) were included in the analysis. Median age and Karnofsky performance status were 59 years (range, 39–84 years) and 90 (range, 40–100), respectively. Tumor volumes and maximum diameters ranged from 0.08 to 15.38 cm^3 (median, 3.67 cm^3) and from 3 to 34 mm (median, 18 mm), respectively. The median follow-up period was 329 days (range, 120–1,321 days). Local-control probabilities at 6 and 12 months were 92.1 and 86.7 %, respectively. Overall survival after HFSRT at 6 and 12 months was 85.4 and 64.5 %, respectively. Grade 3 radiation necrosis was observed in one patient according to the Common Terminology Criteria for Adverse Events version 3.0. The patient was successfully managed conservatively. HFSRT for metastatic brain tumors yields high local-control probabilities without increasing severe adverse events despite high risk factors.

Keywords Metastatic brain tumors · Hypofractionated · Stereotactic radiotherapy · Local control · Toxicity

K. Ogura · T. Mizowaki (✉) · M. Ogura · K. Sakanaka · M. Hiraoka
Department of Radiation Oncology and Image-Applied Therapy, Kyoto University Graduate School of Medicine,
54 Kawahara-cho, Shogoin, Sakyo-ku, Kyoto 606-8507, Japan
e-mail: mizo@kuhp.kyoto-u.ac.jp

Y. Arakawa · S. Miyamoto
Department of Neurosurgery, Kyoto University Graduate School of Medicine, Kyoto, Japan

Introduction

Brain metastases are a commonly reported condition, occurring in 20–40 % of patients with cancer [1]. Brain metastases may be symptomatic and can be the direct cause of death. Brain metastases are primarily treated with open surgery and radiotherapy. Radiotherapy strategies include whole-brain radiotherapy (WBRT) and/or stereotactic irradiation, depending on the clinical situation [2–6]. Stereotactic radiosurgery (SRS) yields high local-control rates for relatively small lesions. However, local control using a single-fraction dose becomes difficult as tumor size increases. Large tumors required a high dose for local control, and exposure of normal brain tissue to a high radiation dose increases the probability of late toxicities such as radiation necrosis [7]. Furthermore, lesions with a history of WBRT

and those located in an eloquent area such as brainstem can increase the probability of the toxicity, because normal brain tissues in these cases probably have a lower tolerance for irradiation and late toxicities should be more problematic in eloquent areas than non-eloquent areas [8]. Survival rates have increased as systemic therapies have improved [1]. More attention should be given to late toxicities under these conditions. Hypofractionated stereotactic radiotherapy (HFSRT) may provide a way to maintain high local-control rates without increasing late toxicities [9, 10]. Recent advances in precision and the development of a less invasive fixation technique have increased the safety of irradiation using a fractionated schedule. The present paper reports the outcome of HFSRT treatment for metastatic brain tumors.

Materials and methods

Patients and tumor characteristics

From June 2008 through July 2011, 39 consecutive patients with 46 brain metastases underwent HFSRT at Kyoto University Hospital. Inclusion criteria included high risk factors such as lesions in eloquent locations, prior history of WBRT, and large tumors (maximum diameter >15 mm). Eloquent lesions are defined as those located at or adjacent to the brainstem, basal ganglion, or motor areas. Of 39 patients, 21 with 27 lesions had follow-up magnetic resonance imaging (MRI) scans at least once 3 months or more after HFSRT and were included in the analysis. The remaining 18 patients could not undergo follow-up MRI scans because of poor performance status. Eligible patient and tumor characteristics are summarized in Table 1. According to the Radiation Therapy Oncology Group (RTOG) recursive partitioning analysis (RPA) [11], the majority of patients in our study (17/21 patients, 81 %) were classified as class II.

Treatment

The treatment was performed using the Novalis system equipped with the ExacTrac system v.5.02 and Robotic Tilt Module mounted on the Exact Couch top (BrainLAB, Feldkirchen, Germany). Patients were immobilized in a thermoplastic stereotactic head mask with an additional bite block and infrared reflecting markers (BrainLAB). Computerized tomography (CT) images of 1.25 mm slice thickness were acquired using a Light Speed RT scanner (GE Healthcare, Milwaukee, WI, USA). Contrast-enhanced MRI scans were also referred with CT-MRI fusion devices. The gross tumor volume (GTV) was defined as the contrast-enhanced lesion detected in CT/MRI images. The clinical target volume (CTV) was defined as being identical to the GTV. The planning target volume (PTV) was formed by expanding the CTV with a 1 mm margin. This margin was evaluated using upfront analysis of the geometric accuracy of frameless stereotactic radiotherapy systems in our hospital [12]. All lesions were treated using a dynamic conformal arc technique with multileaf collimator (MLC) margin 0–1 mm, planned with iPlan RT Dose 4.1.2 (BrainLAB). Three or four arc beams were used. Patients were positioned using the Novalis/ExacTrac system. Positional errors including translations and rotations were corrected by moving the robotic couch. The prescribed doses were specified at the isocenter, and 35 Gy in five fractions was basically prescribed. Brainstem lesions with a prior history of WBRT were treated with lower doses: 20–25 Gy in five fractions was prescribed. PTV was covered by the 80 % isodose line of the prescribed dose to the isocenter. One lesion was exceptionally treated with 40 Gy in five fractions at the discretion of the treating physician.

Follow-up and analysis

After treatment, patients underwent a follow-up MRI scan every 1–3 months, and the maximum diameter of the irradiated lesion in the axial image was measured. Twenty-one patients with 27 lesions had follow-up MRI scans at least once 3 months or more after HFSRT and were eligible for the analysis of local-control probability, probability of developing new brain metastases, overall survival, and time to neurological deterioration in the present study. For the analysis of local control, the response criteria were defined as follows: complete response (CR) was defined as no visible gross tumor or absence of contrast enhancement, partial response (PR) as more than a 30 % decrease in size, progressive disease (PD) as more than a 20 % increase in size, and stable disease (SD) as all other responses. Local control was defined as a status of CR, PR, or SD. Radiation necrosis/injury was defined as lesions in which the contrast-enhanced MRI images were enhanced peripherally or heterogeneously and resulted in no continuous progression on further follow-up. A nuclear medicine study such as positron-emission tomography was conducted as necessary. Open surgery and pathological diagnosis was recommended for lesions that caused clinical symptoms and could not be controlled conservatively. Radiation necrosis was not included in the PD category in the analysis of local control.

Neurologic deterioration was defined a decline in the KPS of $\geq$30 for at least 1 week or a decline in Karnofsky performance status (KPS) from any baseline to $\leq$50 for at least 1 week. If the KPS before HFSRT was <70, neurologic deterioration was defined as any decline in the KPS after HFSRT for at least 1 week. A temporal decline in KPS that was attributable to other causes and not to a neurologic

Table 1 Patient and tumor characteristics

Patient no./tumor no.	Age (years), Gender	KPS	RPA class	Primary tumor	Extracranial lesion and status	Prior WBRT	Tumor location	Eloquent	MD (mm)	PTV (cm^3)	Dose/fr. (Gy)	Local control	Time[a] (day)	Current status
1	61, M	70	II	Lung	Exist/active	Yes	Temporal	No	23	5.98	7	C	95	Dead (systemic)
2	46, F	80	II	Breast	Exist/inactive	No	Cerebellum	No	28	7.11	7	C	404	Alive
3	52, M	90	I	CUP	None	No	Temporal	No	34	11.16	7	C	328	Lost to follow-up
4	66, M	80	II	Lung	Exist/active	Yes	Brainstem	Yes	8	0.30	4	C	181	Dead (systemic)
5	60, F	100	I	Lung	None	Yes	Parietal	No	10	1.04	7	C	461	Alive
6-1	57, F	100	II	Breast	Exist/inactive	Yes	Frontal	No	28	11.40	8	N	1,315	Alive
6-2	58, F	80	II		Exist/inactive	Yes	Cerebellum	No	9	0.44	7	C	711	
7	54, M	100	I	Lung	None	Yes	Cerebellum	No	31	10.08	7	C	526	Alive
8	39, M	80	II	HP	Exist/inactive	No	Frontal	Yes	28	9.78	7	C	138	Dead (systemic)
9	49, F	100	II	Lung	Exist/active	No	Temporal	No	16	2.70	7	R	187	Alive
10-1	74, F	90	II	Lung	Exist/inactive	Yes	Parietal	No	12	1.45	7	C	521	Alive
10-2	74, F	90	II		Exist/inactive	Yes	Brainstem	Yes	8	0.44	5	C	521	
11-1	61, M	80	II	Lung	Exist/inactive	Yes	Temporal	No	27	15.38	7	C	286	Dead (neurologic)
11-2	61, M	80	II		Exist/inactive	Yes	Parietal	Yes	17	2.56	7	C	286	
11-3	62, M	70	II		Exist/inactive	Yes	Temporal	No	19	3.67	7	C	159	
12-1	84, F	40	III	Kidney	Exist/active	No	Brainstem	Yes	3	0.08	7	C	434	Dead (neurologic)
12-2	84, F	40	III		Exist/active	No	Brainstem	Yes	6	0.26	7	R	434	
13	54, F	80	II	Lung	Exist/active	Yes	Cerebellum	No	28	5.79	7	C	92	Dead (systemic)
14	59, F	90	II	Breast	Exist/active	No	Temporal	No	18	5.08	7	C	229	Dead (systemic)
15	71, M	100	II	Lung	Exist/inactive	No	Frontal	No	16	2.49	7	C	715	Alive
16	68, M	90	II	Colon	Exist/active	No	Parietal	Yes	25	4.58	7	R	132	Lost to follow-up
17	68, M	100	II	Lung	Exist/inactive	No	Occipital	No	23	7.13	7	C	280	Alive
18	39, F	100	II	Uterus	Exist/active	No	Temporal	No	28	6.28	7	C	154	Lost to follow-up
19-1	39, F	90	II	Lung	Exist/active	Yes	Frontal	No	13	0.57	7	C	162	Dead (systemic)
19-2	39, F	90	II		Exist/active	Yes	Parietal	No	16	2.05	7	R	92	
20	65, M	90	II	Lung	Exist/inactive	No	Frontal	No	25	6.74	7	C	347	Alive
21	53, M	80	II	Lung	Exist/active	Yes	Brainstem	Yes	13	1.14	5	C	116	Dead (systemic)

C controlled, *CUP* cancer of unknown primary, *F* female, *fr* fraction, *HP* hypopharynx, *KPS* Karnofsky performance status, *M* male, *MD* maximum diameter, *N* radiation necrosis, *PTV* planning target volume, *R* Relapsed, *RPA* Radiation Therapy Oncology Group Recursive Partitioning Analysis, *WBRT* whole-brain radiotherapy

[a] This indicates the time between initiation of hypofractionated stereotactic radiotherapy and progression or last imaging follow-up

deficit was excluded. The cause of death was considered a neurologic cause if the patient had progressive neurologic dysfunction with or without progressive systemic disease.

Statistics

Local-control probability, probability of developing new brain metastases, and overall survival were calculated using the Kaplan–Meier method. The local control probability and the probability of developing new brain metastases were evaluated from the initial HFSRT treatment to the date of failure or last imaging follow-up. Overall survival was measured from the initial HFSRT to the date of death or last follow-up. Time to neurological deterioration was measured from the date of the initial HFSRT to the date of neurological deterioration, death, or last follow-up.

Results

Local control and new lesion development

The median duration of imaging follow-up was 286 days (range, 92–1,315 days). PTV and maximum diameter of the tumor ranged from 0.08 to 15.38 cm^3 (median, 3.67 cm^3) and from 3 to 34 mm (median, 18 mm), respectively. With the exception of the brainstem lesions (5 lesions, 18.5 %), the PTV and maximum diameter were 0.44–15.38 cm^3 (median, 5.44 cm^3) and 9–34 mm (median, 23 mm), respectively. Brainstem lesions are more likely to be symptomatic and lethal than lesions in other locations, even when they are relatively small [13]; thus, we treated the brainstem lesions as soon as possible. Of the 21 patients, 10 (47.6 %) with 15 of the 27 lesions (55.6 %) had a history of WBRT before receiving HFSRT. The time between the end of prior WBRT and the initiation of HFSRT was 563 days (69–1,116 days). The dose fractionation of prior WBRT was 30 Gy in 10 fractions (7 patients), 37.5 Gy in 15 fractions (2 patients), and 25 Gy in 10 fractions (1 patient). All these patients underwent HFSRT as salvage for failed WBRT.

The local-control probabilities were 92.1 % [95 % confidence interval (CI), 82.2–100] at 6 months and 86.7 % (95 % CI, 73.5–100) at 12 months (Fig. 1a). At the time of analysis, four lesions in four patients were diagnosed as PD (Table 1). All PD lesions had been treated with an irradiation schedule of 35 Gy in five fractions.

Eleven patients (52.4 %) had new brain metastases after the initial HFSRT treatment. The probability of developing new brain metastases was 45.4 % (95 % CI, 18.1–63.6) at 6 months and 59.0 % (95 % CI, 27.6–76.8) at 12 months (Fig. 1b).

Toxicity

According to the Common Terminology Criteria for Adverse Events version 3.0, no grade 3–4 acute toxicities occurred in our study. Two grade 2 seizures were observed: one transient partial convulsion and one general seizure. Grade 2 mild hemorrhages at the irradiated site were observed in three patients, and they were successfully managed conservatively. We observed late toxicity in one patient, who developed a grade 3 radiation necrosis associated with clinical symptoms. The patient had a metastatic tumor in the right frontal lobe derived from breast cancer. The tumor was treated with 40 Gy in five fractions. The patient had a history of WBRT (30 Gy in 10 fractions) performed 15 months prior to the HFSRT. Initially, the tumor appeared to gradually shrink, but the contrast-enhanced lesion emerged approximately 2 years after HFSRT with clinical symptoms, increased weakness, and gait impairment. Surgery was recommended by a specialized neurosurgeon, but the patient refused and was treated with conservative therapy. At present, the symptoms have improved, and the enhanced areas and surrounding edema have disappeared.

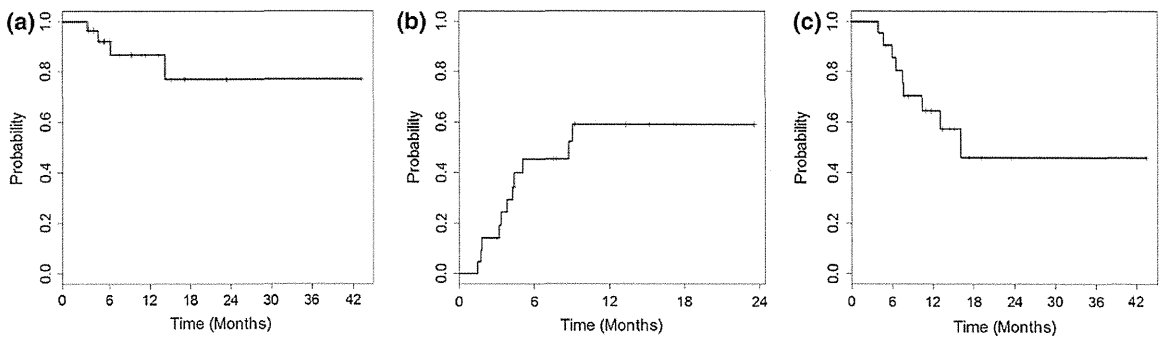

Fig. 1 **a** Local-control probability, **b** probability of developing new brain metastases, and **c** overall survival estimated using the Kaplan–Meier method

Overall survival and time to neurological deterioration

The median follow-up after HFSRT was 329 days (range, 120–1,321 days). Overall survival was 85.4 % (95 % CI, 71.5–100) at 6 months and 64.5 % (95 % CI, 46.3–89.8) at 12 months (Fig. 1c). Time to neurological deterioration was a median of 316 days (range, 98–1,011 days).

Nine patients had died at the time of analysis. The cause of death was neurologic causes in four patients and progressive systemic cancer in five patients. Another three patients were lost to follow-up, and all had progressive intracranial diseases and neurologic dysfunction. The remaining nine patients are alive to date and all except one is free from neurologic symptoms. The one patient had neurologic deterioration due to progressive intracranial disease.

As to the seven patients with eight eloquent lesions, time to neurological deterioration was a median of 231 days (range, 98–651 days) after the initiation of HFSRT. Of them, four patients had one or two lesion(s) at the brainstem and three patients had a history of WBRT (30 Gy in 10 fractions). The intervals between the end of WBRT and the initiation of HFSRT were 69, 171, and 325 days. Three improved or had stable neurologic symptoms at the time of last follow-up: two had stable or improved oculomotor nerve impairment and one had no neurologic symptoms. The other had local brainstem failure at 434 days after HFSRT and also had rapidly growing multiple intracranial lesions that caused neurologic deterioration. In contrast, two of three patients with lesions at the motor area had no severe acute toxicity but had neurologic deterioration due to local or other progressive lesions within the brain.

Discussion

Research in the 1990s suggested that hypofractionation had significant benefits over single-dose radiosurgery in terms of widening the therapeutic window between tumor control and late effects, particularly for malignant tumors [9, 10]. Current noninvasive, sophisticated techniques such as HFSRT have enabled clinicians to deliver high radiation doses to lesions precisely and repeatedly.

Dose escalation using single-fraction radiosurgery is problematic because large tumors require high doses that may cause late neurological toxicities. The first dose-escalation study using single-fraction radiosurgery (Radiation Therapy Oncology Group Study 90-05; RTOG 90-05) [7] was conducted to establish the maximum tolerable dose for patients with recurrent, previously irradiated, primary brain tumors, and brain metastases. Doses were prescribed to the 50–90 % isodose line according to the maximum diameter of the tumor. The results showed that the maximum tolerable doses for SRS were 24, 18, and 15 Gy for tumors with maximum diameters $\leq$20, 21–30, and 31–40 mm, respectively. Thus, the dose for larger tumors was reduced when using single-dose SRS, although dose escalation would be desirable in terms of controlling larger tumors.

In daily clinical practice, lesions amenable to SRS are typically <3 cm in maximum diameter [14], and local control has been reported to be influenced by tumor size [15–18]. However, the relationship between tumor size and local control is difficult to assess because lower doses are prescribed for larger tumors and higher doses for smaller ones. Thus, the relationship between tumor size and local control in relation to one fixed dose in a single fraction is not clear and is seldom addressed in the literature. For relatively small tumors $\leq$2 cm, many reports have shown good local control rates by using single-fraction SRS [14]. However, a cut-off value for local control seems to exist in even small tumors $\leq$2 cm. To our knowledge, there are two reports regarding this point of view [19, 20]. One study by Chang et al. [19] showed that the threshold value was a maximum tumor diameter of 1 cm. The maximum diameter of the treated lesions in that study was 2.1 cm, and they were treated in a single fraction with a prescribed dose of 20–24 Gy to the periphery of the target. Chang and colleagues reported that the 1 year local-control rates were 86 % in tumors with a diameter $\leq$1 cm and 56 % in tumors with a diameter >1 cm [19]. The local-control rates found in the larger-diameter group were low compared with previously reported rates [14], which may have been due to the authors' criteria for inclusion and local treatment failure. The other study by Shehata et al. [20] reported excellent local control with single-fraction SRS for $\leq$2 cm tumors. At the same time, they also found that tumor volume was a significant factor affecting tumor control in their multivariate analysis. The threshold value was 0.3 cm^3, which was equal to about 0.8 cm estimated diameter.

Evidence suggests that hypofractionation could overcome the disadvantages of single-fraction radiosurgery. Several investigators have reported good results for local control using various hypofractionation schedules [21–29]. We also achieved high local-control rates of 92.1 and 86.7 % at 6 and 12 months, respectively, despite relatively large tumor diameters (median, 18 mm), and four relapsed cases (Table 1), which were irradiated with 35 Gy in five fractions. Two of the tumors were derived from colon and renal cancers, which were thought to be radioresistant tumors. Additionally, all four patients with these lesions had uncontrolled extracranial lesions, and these unfavorable factors might be associated with undesirable outcomes, but the actual relationship between local control and its predictive factors was not clear in the present study. An increase in dose escalation may be necessary to obtain better local-control probabilities; however, our sample size was too small to confirm this notion.

Optimal fractionation schedules need to be determined. Wiggenraad et al. [29] conducted a systematic review of stereotactic fractionated radiotherapy in metastatic brain tumors using a modified linear–quadratic–cubic (LQC) model. The LQC model adjusted the LQ model to account for a more linear response at higher doses by adding an additional term proportional to the cube of the dose. They concluded that a biologically effective dose at an α/β value of 12 Gy (BED_{12}) of at least 40 Gy was needed for a 12 month local-control rate of 70 % or greater. Most of the patients in our study received a dose of 35 Gy in five fractions. Using a classical LQ model, the BED_{12} of this dose fractionation is significantly lower than that of single dose fraction radiosurgery. For example, the BED_{12} of 25 Gy in a single fraction is 77.1 Gy according to the classical LQ model, and 35 Gy in five fractions corresponds to a BED_{12} of 55.4 Gy. However, using the LQC model, both dose fractionations are the same, estimated as $BED_{12} = 53.0$ Gy. The peripheral doses of PTV, 80 % of the prescribed dose at the isocenter, were 28 Gy in five fractions and 20 Gy in a single fraction. Both were calculated as a BED_{12} of 40 Gy. Thus, we obtained good local-control rates in our study, supporting the notion of a more linear response rate between cell survival and dose at higher doses. Application of the LQC model to clinical practice is reasonable when comparing the BED_{12} of HFSRT with that of SRS at high doses. Lower doses estimated using the classical LQ model should provide good local control of metastatic brain tumors despite large sizes.

The role of tumor size in the control of brain metastases was not clear in the present study. Aoyama et al. [23] reported tumor volume > 3 cm^3 (equal to about 1.8 cm estimated diameter) is a significant prognostic factor for local control. However, some aspects of their study were different from ours, as follows: a fractionation schedule of 20–40 Gy in four fractions at the isocenter, setup accuracy and PTV margin of 2 mm, and dose delivery without MLC. To our knowledge, no other study has described the relationship between tumor size and local control in HFSRT. We think that the rationale behind better local control in HFSRT is safe dose escalation for larger tumors and radiobiological benefit of fractionation. According to the LQC model, HFSRT enables delivery of the same effective doses for larger tumors as a high-single dose for smaller tumors. In addition, some radiobiological benefit, such as reoxygenation, also contributes to better outcomes. The interval between each fractionated dose allows hypoxic tumor cells to be aerobic and radiosensitive, and to be killed by subsequent dose fractions [10]. The maximum diameter in the present study was up to 34 mm. Tumors within this range seem to be safely controlled and a cutoff may exist at much larger sizes. However, HFSRT for much larger tumors would be a remaining issue for the future evaluations.

Late toxicities such as radiation necrosis and radiation injury may be life-threatening. The exact rates of radiation necrosis are not known. One reason for this is the difficulty in differentiating between a radiation injury and a recurrence [30]. Few studies describe the method used to distinguish a radiation necrosis from a true recurrence in their analysis of local control in brain metastases. The judgment appears to be based on clinical factors in most studies, and many report crude rates of radiation necrosis of 5–10 % [29]. In the RTOG 90-05 study, radiation necrosis was frequently observed when large-volume tumors were irradiated with high doses that were not clinically tolerated. In our study, the crude rate of radiation necrosis was 3.7 % (one lesion), which occurred in the lesion irradiated with a dose of 40 Gy in five fractions. This patient had a history of WBRT, 30 Gy in 10 fractions. Radiation necrosis was not observed in other lesions in our study in those treated with 20–35 Gy in five fractions, even though half of them had been previously irradiated with WBRT. Moreover, with the exception of lesions in the brainstem, the median PTV was relatively large (median, 5.44 cm^3); however, we did not observe severe toxicity.

To our knowledge, no reports have shown a direct comparison of the incidence of radiation necrosis between WBRT plus SRS and SRS alone. However, we have some suggestive data in the Japanese randomized controlled trial [5]. In this trial, 132 patients with one to four metastases, each less than 3 cm in diameter, were randomly assigned to receive up-front WBRT plus SRS (65 patients) or SRS alone (67 patients). As a result, more patients treated with SRS plus WBRT developed radiation necrosis (three patients) than patients treated with SRS alone (one patient), although the SRS dose was reduced by 30 % in SRS plus WBRT group compared with SRS alone group. This observation suggests WBRT followed by SRS may result in increasing the risk of radiation necrosis.

A reduction in late toxicity is crucial for long-term survival. Patients with primary tumors such as renal cancer have been reported to have longer survival times than patients with other primary tumors [22], and more investigations should focus on the longer-surviving patients. Varlotto et al. [31] reported that the actuarial incidence of adverse events at 1 and 5 years was 2.8 and 11.4 %, respectively, in patients who had survived at least 1 year after radiosurgery for brain metastases. In our study, nine patients survived more than 1 year after HFSRT. One patient, who was treated with 40 Gy in five fractions, developed radiation necrosis. The sample size in our study was small, but 35 Gy in five fractions appears to be a safe dose.

The small sample size in the present study and limitations imposed by retrospective analyses do not allow us to

definitively state that metastatic tumor treatment with HFSRT is superior to SRS. However, a randomized trial to compare these two methods would be unethical considering the toxicity of the higher doses in SRS. Nonetheless, a prospective study to determine optimal dose and fractionation schedules is warranted. Our results demonstrate the potential of HFSRT in terms of tumor-control probability and reduction in toxicities as a treatment for metastatic brain tumors with high risk factors.

Conclusions

We conclude that HFSRT is safe and produces high local-control rates for metastatic brain tumors with high risk factors. We will continue to use this fractionation schedule for these difficult cases and conduct long-term follow-up to evaluate the efficacy of this strategy.

Acknowledgment This work was supported in part by Grants-in-Aid for Scientific Research from the Ministry of Education, Culture, Sports, Science, and Technology of Japan (20229009).

References

1. Soffietti R, Ruda R, Trevisan E (2008) Brain metastases: current management and new developments. Curr Opin Oncol 20:676–684. doi:10.1097/CCO.0b013e32831186fe
2. Patchell RA, Tibbs PA, Regine WF, Dempsey RJ, Mohiuddin M, Kryscio RJ, Markesbery WR, Foon KA, Young B (1998) Post-operative radiotherapy in the treatment of single metastases to the brain: a randomized trial. JAMA 280:1485–1489
3. Patchell RA, Tibbs PA, Walsh JW, Dempsey RJ, Maruyama Y, Kryscio RJ, Markesbery WR, Macdonald JS, Young B (1990) A randomized trial of surgery in the treatment of single metastases to the brain. N Engl J Med 322:494–500. doi:10.1056/NEJM199002223220802
4. Andrews DW, Scott CB, Sperduto PW, Flanders AE, Gaspar LE, Schell MC, Werner-Wasik M, Demas W, Ryu J, Bahary JP, Souhami L, Rotman M, Mehta MP, Curran WJ Jr (2004) Whole brain radiation therapy with or without stereotactic radiosurgery boost for patients with one to three brain metastases: phase III results of the RTOG 9508 randomised trial. Lancet 363:1665–1672. doi:10.1016/S0140-6736(04)16250-8
5. Aoyama H, Shirato H, Tago M, Nakagawa K, Toyoda T, Hatano K, Kenjyo M, Oya N, Hirota S, Shioura H, Kunieda E, Inomata T, Hayakawa K, Katoh N, Kobashi G (2006) Stereotactic radiosurgery plus whole-brain radiation therapy vs stereotactic radiosurgery alone for treatment of brain metastases: a randomized controlled trial. JAMA 295:2483–2491. doi:10.1001/jama.295.21.2483
6. Kocher M, Soffietti R, Abacioglu U, Villa S, Fauchon F, Baumert BG, Fariselli L, Tzuk-Shina T, Kortmann RD, Carrie C, Ben Hassel M, Kouri M, Valeinis E, van den Berge D, Collette S, Collette L, Mueller RP (2011) Adjuvant whole-brain radiotherapy versus observation after radiosurgery or surgical resection of one to three cerebral metastases: results of the EORTC 22952–26001 study. J Clin Oncol 29:134–141. doi:10.1200/JCO.2010.30.1655
7. Shaw E, Scott C, Souhami L, Dinapoli R, Kline R, Loeffler J, Farnan N (2000) Single dose radiosurgical treatment of recurrent previously irradiated primary brain tumors and brain metastases: final report of RTOG protocol 90–05. Int J Radiat Oncol Biol Phys 47:291–298
8. Williams BJ, Suki D, Fox BD, Pelloski CE, Maldaun MV, Sawaya RE, Lang FF, Rao G (2009) Stereotactic radiosurgery for metastatic brain tumors: a comprehensive review of complications. J Neurosurg 111:439–448. doi:10.3171/2008.11.JNS08984
9. Brenner DJ, Martel MK, Hall EJ (1991) Fractionated regimens for stereotactic radiotherapy of recurrent tumors in the brain. Int J Radiat Oncol Biol Phys 21:819–824
10. Hall EJ, Brenner DJ (1993) The radiobiology of radiosurgery: rationale for different treatment regimes for AVMs and malignancies. Int J Radiat Oncol Biol Phys 25:381–385
11. Gaspar L, Scott C, Rotman M, Asbell S, Phillips T, Wasserman T, McKenna WG, Byhardt R (1997) Recursive partitioning analysis (RPA) of prognostic factors in three Radiation Therapy Oncology Group (RTOG) brain metastases trials. Int J Radiat Oncol Biol Phys 37:745–751
12. Takakura T, Mizowaki T, Nakata M, Yano S, Fujimoto T, Miyabe Y, Nakamura M, Hiraoka M (2010) The geometric accuracy of frameless stereotactic radiosurgery using a 6D robotic couch system. Phys Med Biol 55:1–10. doi:10.1088/0031-9155/55/1/001
13. Kelly PJ, Lin YB, Yu AY, Ropper AE, Nguyen PL, Marcus KJ, Hacker FL, Weiss SE (2011) Linear accelerator-based stereotactic radiosurgery for brainstem metastases: the Dana-Farber/Brigham and Women's Cancer Center experience. J Neurooncol 104:553–557. doi:10.1007/s11060-010-0514-0
14. Linskey ME, Andrews DW, Asher AL, Burri SH, Kondziolka D, Robinson PD, Ammirati M, Cobbs CS, Gaspar LE, Loeffler JS, McDermott M, Mehta MP, Mikkelsen T, Olson JJ, Paleologos NA, Patchell RA, Ryken TC, Kalkanis SN (2010) The role of stereotactic radiosurgery in the management of patients with newly diagnosed brain metastases: a systematic review and evidence-based clinical practice guideline. J Neurooncol 96:45–68. doi:10.1007/s11060-009-0073-4
15. Matsuo T, Shibata S, Yasunaga A, Iwanaga M, Mori K, Shimizu T, Hayashi N, Ochi M, Hayashi K (1999) Dose optimization and indication of Linac radiosurgery for brain metastases. Int J Radiat Oncol Biol Phys 45:931–939
16. Vogelbaum MA, Angelov L, Lee SY, Li L, Barnett GH, Suh JH (2006) Local control of brain metastases by stereotactic radiosurgery in relation to dose to the tumor margin. J Neurosurg 104:907–912. doi:10.3171/jns.2006.104.6.907
17. Schomas DA, Roeske JC, MacDonald RL, Sweeney PJ, Mehta N, Mundt AJ (2005) Predictors of tumor control in patients treated with linac-based stereotactic radiosurgery for metastatic disease to the brain. Am J Clin Oncol 28:180–187
18. Molenaar R, Wiggenraad R, Verbeek-de Kanter A, Walchenbach R, Vecht C (2009) Relationship between volume, dose and local control in stereotactic radiosurgery of brain metastasis. Br J Neurosurg 23:170–178. doi:10.1080/02688690902755613
19. Chang EL, Hassenbusch SJ III, Shiu AS, Lang FF, Allen PK, Sawaya R, Maor MH (2003) The role of tumor size in the radiosurgical management of patients with ambiguous brain metastases. Neurosurgery 53:272–280, discussion 280–281
20. Shehata MK, Young B, Reid B, Patchell RA, St Clair W, Sims J, Sanders M, Meigooni A, Mohiuddin M, Regine WF (2004) Stereotatic radiosurgery of 468 brain metastases < or =2 cm: implications for SRS dose and whole brain radiation therapy. Int J Radiat Oncol Biol Phys 59:87–93. doi:10.1016/j.ijrobp.2003.10.009
21. Manning MA, Cardinale RM, Benedict SH, Kavanagh BD, Zwicker RD, Amir C, Broaddus WC (2000) Hypofractionated

stereotactic radiotherapy as an alternative to radiosurgery for the treatment of patients with brain metastases. Int J Radiat Oncol Biol Phys 47:603–608
22. Ikushima H, Tokuuye K, Sumi M, Kagami Y, Murayama S, Ikeda H, Tanaka M, Oyama H, Shibui S, Nomura K (2000) Fractionated stereotactic radiotherapy of brain metastases from renal cell carcinoma. Int J Radiat Oncol Biol Phys 48:1389–1393
23. Aoyama H, Shirato H, Onimaru R, Kagei K, Ikeda J, Ishii N, Sawamura Y, Miyasaka K (2003) Hypofractionated stereotactic radiotherapy alone without whole-brain irradiation for patients with solitary and oligo brain metastasis using noninvasive fixation of the skull. Int J Radiat Oncol Biol Phys 56:793–800
24. Ernst-Stecken A, Ganslandt O, Lambrecht U, Sauer R, Grabenbauer G (2006) Phase II trial of hypofractionated stereotactic radiotherapy for brain metastases: results and toxicity. Radiother Oncol 81:18–24. doi:10.1016/j.radonc.2006.08.024
25. Narayana A, Chang J, Yenice K, Chan K, Lymberis S, Brennan C, Gutin PH (2007) Hypofractionated stereotactic radiotherapy using intensity-modulated radiotherapy in patients with one or two brain metastases. Stereotact Funct Neurosurg 85:82–87. doi:10.1159/000097923
26. Fahrig A, Ganslandt O, Lambrecht U, Grabenbauer G, Kleinert G, Sauer R, Hamm K (2007) Hypofractionated stereotactic radiotherapy for brain metastases—results from three different dose concepts. Strahlenther Onkol 183:625–630. doi:10.1007/s00066-007-1714-1
27. Kwon AK, Dibiase SJ, Wang B, Hughes SL, Milcarek B, Zhu Y (2009) Hypofractionated stereotactic radiotherapy for the treatment of brain metastases. Cancer 115:890–898. doi:10.1002/cncr.24082
28. Kim YJ, Cho KH, Kim JY, Lim YK, Min HS, Lee SH, Kim HJ, Gwak HS, Yoo H (2011) Single-dose versus fractionated stereotactic radiotherapy for brain metastases. Int J Radiat Oncol Biol Phys 81:483–489. doi:10.1016/j.ijrobp.2010.05.033
29. Wiggenraad R, Verbeek-de Kanter A, Kal HB, Taphoorn M, Vissers T, Struikmans H (2011) Dose-effect relation in stereotactic radiotherapy for brain metastases. A systematic review. Radiother Oncol 98:292–297. doi:10.1016/j.radonc.2011.01.011
30. Soussain C, Ricard D, Fike JR, Mazeron JJ, Psimaras D, Delattre JY (2009) CNS complications of radiotherapy and chemotherapy. Lancet 374:1639–1651. doi:10.1016/S0140-6736(09)61299-X
31. Varlotto JM, Flickinger JC, Niranjan A, Bhatnagar AK, Kondziolka D, Lunsford LD (2003) Analysis of tumor control and toxicity in patients who have survived at least one year after radiosurgery for brain metastases. Int J Radiat Oncol Biol Phys 57:452–464

IDH1/2 mutation is a prognostic marker for survival and predicts response to chemotherapy for grade II gliomas concomitantly treated with radiation therapy

YOSHIKO OKITA[1], YOSHITAKA NARITA[1], YASUJI MIYAKITA[1], MAKOTO OHNO[1], YUKO MATSUSHITA[1], SHINTARO FUKUSHIMA[2], MINAKO SUMI[3], KOICHI ICHIMURA[4], TAKAMASA KAYAMA[1] and SOICHIRO SHIBUI[1]

Departments of [1]Neurosurgery and Neuro-Oncology, [2]Pathology and Clinical Laboratories and [3]Radiation Oncology, [4]Division of Brain Tumor Translational Research, National Cancer Center, Tokyo 104-0045, Japan

Received April 27, 2012; Accepted June 29, 2012

DOI: 10.3892/ijo.2012.1564

Abstract. Reliable prognostic biomarkers of grade II gliomas remain unclear. This study aimed to examine the role of mutations of isocitrate dehydrogenase (*IDH1/2*), 1p/19q co-deletion, and clinicopathological factors in patients with grade II glioma who were primarily treated with radiotherapy or chemoradiotherapy after surgery. Seventy-two consecutive patients, including 49 cases of diffuse astrocytomas (DA), 4 oligodendrogliomas (OL) and 19 oligoastrocytomas (OA), who underwent treatment from 1991 to 2010 at a single institution were examined. The overall survival (OS) of the DA patients (8.3 years) was significantly shorter than that of the OL and OA patients (11.7 years). *IDH1/2* mutations were found in 46.9% of the DA patients and 82.6% of the OL and OA patients. The progression-free survival (PFS) and OS of the patients with *IDH1/2* mutations (8.4 and 16.3 years) were significantly longer than those of the patients without *IDH1/2* mutations (3.3 and 4.5 years). Among the patients with *IDH1/2* mutations, those who were initially treated with chemoradiotherapy including nimustine hydrochloride (ACNU), had significantly longer PFS than those treated with radiotherapy alone, whereas no significant difference in PFS was observed between the chemoradiotherapy and radiotherapy groups in the patients without *IDH1/2* mutations. Oligodendroglial tumors, age <40 years, initial Karnofsky performance status (KPS) ≥80, and *IDH1/2* mutations were favorable prognostic factors regarding PFS and OS. *IDH1/2* mutation was a predictive factor of response to chemoradiotherapy in grade II gliomas. Patients with *IDH1/2* mutations may benefit more from chemoraiotherapy than those without *IDH1/2* mutations.

Correspondence to: Dr Yoshitaka Narita, Department of Neurosurgery and Neuro-Oncology, National Cancer Center Hospital, 5-1-1 Tsukiji, Chuo-ku, Tokyo 104-0045, Japan
E-mail: yonarita@ncc.go.jp

Key words: grade II gliomas, *isocitrate dehydrogenase 1*, *isocitrate dehydrogenase* 2, 1p/19q codeletion, chemoradiotherapy, diffuse astrocytoma

Introduction

World Health Organization (WHO) grade II gliomas (low-grade gliomas) are slow-growing tumors that include several subtypes, such as diffuse astrocytomas, mixed oligoastrocytomas, and oligodendrogliomas (1). The 10- and 20-year survival rates for patients with grade II glioma are reported to be 48 and 22% (2), reflecting the malignant potential of these tumors in long-term survival. Radiotherapy is often the treatment of choice for patients with incompletely resected grade II gliomas. However, the timing of radiotherapy for patients with these malignancies remains controversial and no difference in overall survival (OS) between groups receiving early and delayed radiation has been reported (3). Moreover, the efficacy of chemoradiotherapy for grade II gliomas is largely unknown. The addition of procarbazine, lomustine, and vincristine (PCV) therapy to radiotherapy for grade II gliomas conferred a significant increase in OS and progression-free survival (PFS) of >2 years in the Radiation Therapy Oncology Group (RTOG) 9802 study (4), suggesting that chemoradiotherapy might be effective for a subset of these patients.

Several studies have attempted to identify prognostic factors for grade II gliomas. To date, older age, astrocytic histology, the presence of neurologic deficits before surgery, larger tumor diameters, and tumors crossing the midline have been proposed as unfavorable prognostic factors (5-9). Several genetic markers, such as 1p/19q codeletion or mutations of the isocitrate dehydrogenase 1 and 2 genes (*IDH1/2*), have also been associated with patient survival. Oligodendrogliomas typically show 1p/19q codeletion (≤70%) (10,11), and its presence is reported to predict longer survival in oligodendroglial tumors (12). The 1p/19q codeletion is also a statistically significant predictor of prolonged survival in patients with astrocytomas (13). Furthermore, 1p/19q codeletion was associated with longer survival in all types of adult gliomas, independent of age and diagnosis (14,15). On the other hand, 1p/19q codeletion did not appear to be a sensitive prognostic biomarker in patients with either grade II astrocytic